

TECHNISCHE UNIVERSITEIT DELFT

Master Thesis

---

# Magnetic field resilient lumped element superconducting resonators

---

*Author:*

David Feldstein Bofill

*Supervisors:*

Marta Pita Vidal

Prof. dr. Christian K. Andersen

Topological cQED group, QuTech  
Delft, The Netherlands, April 2022



# Contents

List of main variables and abbreviations . . . . .	i
Abstract . . . . .	ii
Acknowledgements . . . . .	iii
<b>1 Introduction</b>	<b>1</b>
<b>2 Physics behind superconducting circuits</b>	<b>3</b>
2.1 Superconductivity . . . . .	3
2.2 Conductivity of normal metals . . . . .	4
2.3 Zero resistance and Meissner effect . . . . .	5
2.4 Internal inductance: Kinetic and magnetic . . . . .	7
2.5 Microscopic theory of superconductivity . . . . .	9
2.5.1 Kinetic inductance from BCS theory . . . . .	10
2.6 Kinetic and magnetic inductance of CPW . . . . .	11
2.7 Material losses in superconducting resonators . . . . .	12
2.7.1 Two-level systems loss . . . . .	12
2.7.2 Magnetic vortices loss . . . . .	13
2.7.3 Quasiparticles loss . . . . .	13
2.7.4 Radiation loss . . . . .	14
2.7.5 Loss uncertainty . . . . .	14
<b>3 Engineering behind microwave circuits</b>	<b>15</b>
3.1 Lumped elements in microwave circuits . . . . .	15
3.1.1 Lumped-element circuit model for a transmission line . . . . .	15
3.1.2 Design of microwave lumped elements . . . . .	17
3.2 Modelling of Resonator circuits . . . . .	23
3.2.1 Circuit model . . . . .	23
3.2.2 Unloaded parallel RLC circuit . . . . .	23
3.2.3 Loaded parallel RLC circuit . . . . .	25
3.2.4 Transmission of a parallel RLC resonator . . . . .	26

3.2.5	Number of photons in the resonator . . . . .	28
<b>4</b>	<b>Design and Fabrication</b>	<b>29</b>
4.1	General design of a superconducting lumped element resonator . . . . .	29
4.1.1	Artificial pinning sites . . . . .	30
4.2	Simulation approach . . . . .	31
4.3	Chip designs . . . . .	34
4.3.1	Design 1: 10 resonator inductor's width dependence . . . . .	35
4.3.2	Design 2: 10 resonator capacitor's size dependence . . . . .	36
4.3.3	Design 3: 10 resonator gap dependence . . . . .	37
4.3.4	Design 4: 10 resonator capacitor's edge dependence . . . . .	37
4.4	Device Fabrication . . . . .	38
<b>5</b>	<b>Measurement Setup</b>	<b>39</b>
5.1	Measurement procedure . . . . .	39
5.2	Field alignment . . . . .	43
<b>6</b>	<b>Measurement Results</b>	<b>45</b>
6.1	Zero field transmission measurements . . . . .	45
6.2	Geometry dependence at zero field . . . . .	46
6.3	Power dependence of SC resonators . . . . .	47
6.4	Magnetic Field . . . . .	49
6.4.1	Parallel Magnetic Field . . . . .	49
6.4.2	Perpendicular Magnetic Field . . . . .	52
<b>7</b>	<b>Conclusions and further research</b>	<b>55</b>
7.1	Outlook . . . . .	56
<b>A</b>	<b>Appendix A Coupling Quality factor</b>	<b>57</b>
<b>B</b>	<b>Appendix B Fabrication recipe</b>	<b>59</b>
B.1	Wafer . . . . .	59
B.1.1	Deposition . . . . .	59
B.1.2	Markers . . . . .	59
B.2	Chip . . . . .	60
B.2.1	Sample cleaning . . . . .	60
B.2.2	Lithography . . . . .	60
B.2.3	Development . . . . .	60
B.2.4	Dry Etching . . . . .	60
B.2.5	Dicing . . . . .	60

B.2.6	Wire Bonding . . . . .	61
B.2.7	Optical micrographs . . . . .	61
B.2.8	SEM inspection . . . . .	61
<b>Appendix C</b>	<b>Additional Measurements</b>	<b>63</b>
<b>Bibliography</b>		<b>76</b>



## List of main variables and abbreviations

- $L_k$ : Kinetic inductance
- $L_m$ : Magnetic inductance
- $C$ : Capacitance
- $C_c$ : Coupling capacitance
- NbTiN: Niobium Titanium Nitride
- T: Temperature
- $Q_T$ : Total quality factor
- $Q_c$ : Coupling quality factor
- $Q_i$ : Internal quality factor
- $\omega$ : Frequency in rad/s
- $f$ : Frequency in Hz
- $f_r$ : Resonance frequency
- $g_r$ : Gap capacitor-to-ground
- $W_r$ : Inductor's width
- $R_r$ : Capacitor's edge radius
- $L_r$ : Capacitor's size
- $s_r$ : Spacing between the resonator and the feedline
- CPW: Coplanar Waveguide

# Abstract

The aim of this thesis is to investigate the role of lumped element resonator geometry in its quality factor. That is how to optimize the resonator's design for enhanced performance of the resonator even in the presence of applied magnetic fields.

Our device comprises a superconducting NbTiN thin film on top of a high resistivity silicon substrate, patterned with a feedline capacitively coupled to ten lumped element resonators aiming to characterize one geometric parameter. The first result of this thesis is the dependence of the intrinsic quality factor on resonator geometry at zero field. The second result is the power dependence for every resonator, with whom we obtain access to the various loss mechanisms degrading the resonator's performance. Finally in plane and out plane magnetic field measurements are presented and a comparison with geometry is discussed. The dominant loss mechanism observed in all resonators stems from quasiparticle loss due to microwave induced pair-breaking. Wide inductor resonators show to be the most susceptible to this loss form. The extracted quality factors at zero field show no correlation with capacitor's geometry within measurement variability, but could potentially show that thin inductors have higher quality factors. In the presence of an applied parallel magnetic field, we find that small capacitors perform better than large capacitors as the field increases. However, we find no additional trend between parallel field and resonator's geometry. Analyzing the behaviour of the resonators under an applied perpendicular magnetic field, we find that thin inductors and small capacitors are features of the most resilient resonators up to at least 100mT, while capacitor's shape does not show any conclusive trend. As a result, our lumped-element resonators prove to be resilient to perpendicular magnetic fields up to at least 100mT with a very simple design and fabrication process.

## Acknowledgements

This work represents the final academic part of my studies at TU Delft. Upon concluding this journey I realize it has only been possible thanks to incredible people I have met along the way. During this period of time I have developed as a researcher, teacher, and hopefully I have become a more resourceful person. I truly believe I will apply the acquired knowledge in my future work. I chose a thesis in qubit research motivated by the idea of participating in the quantum computing progress and the invaluable impact it can have in our society, and I am extremely happy to have enjoyed the actual work it entailed.

First, I would like to express my most sincere gratitude to my supervisor Prof. Dr. Christian K. Andersen. Besides his counseling in all the technical aspects, his questions always helped me gain more insight on the matter and guide my research accordingly. I would like to thank the invaluable help of Marta Pita Vidal, an exceptional researcher to whom I owe everything I know in this field, from simulations and clean room fabrication to cryo-measurements. She has answered every little question I have had in every step of the way, while providing me with tools to progress on my own.

My sincere thanks to Prof. Dr. Leo K., for giving me the opportunity to work in such a warm and outstanding group. I really appreciate the discussions and advice from the Topo-cQED team, Arno, Jaap, Lukas S. and Lukas G. And, Pepijn, for making the office room a friendly place and offering me the chance to talk about non-physics topics.

I am fortunate for the people who has accompanied me throughout this process. A great amount of gratitude goes to my friends, old and new, long distance and next door, who reminded me of the outside world and made me live unforgettable stories.

Finalment, gràcies Laura per les infinites trucades i escoltar tot el que t'explico, en deus saber tant com jo ja. Sóc molt afortunat de tenir una família que m'ha acompanyat sense esperar res a canvi, Papa, Mama, gràcies per aquesta experiència i estar al meu costat.



Everyone has the right to doubt  
everything as often as he pleases  
and the duty to do it at least once.  
No way of looking at things is too  
sacred to be reconsidered. No way  
of doing things is beyond  
improvement.

---

*Edward de Bono*

# Chapter 1

## Introduction

Over the last decades, superconducting circuits have been of great interest to different areas of research. In particular the superconducting microwave resonator has proved to be a multi-purpose component suitable for many applications. On one hand superconducting resonators have been used as low temperature light-detectors by the astronomy community [1]. In quantum computing the resonator has been used for qubit protection and readout [2] [3], coupling of qubit-qubit [4] and in the field of quantum memories [5]. In order to extend qubit coherence times and study qubit performance in magnetic fields the use of superconducting resonators has been fundamental, since the single-photon power operating regime of qubits do not allow them to investigate material loss mechanisms [6]. It is these loss mechanisms that produce unwanted relaxation of the qubit via the Purcell effect [7] and minimize two-qubit gate fidelities [8].

Resonators are useful structures due to their simplicity in modelling, design, fabrication and measurement. They can be measured over a wide range of frequencies, power and temperatures, making them convenient for many experiments. Recently, superconducting resonators started being used to investigate microscopic phenomena which require applied magnetic fields of the order of 1T, such as Majorana physics. For this kind of applications it is important that resonators maintain high quality factors in the presence of magnetic fields. Initially CPW resonators were widely used [9] due to their simplicity in design and scalability, however their large on-chip footprint made them more susceptible to applied magnetic fields [10]. As a result new types of field-resilient resonators were required. Samkharadze [11] introduced nanowire resonators which proved to be very robust to applied fields. Nonetheless their long and narrow geometry lead to a challenging fabrication, strong sensitivity of the resonance frequency to the film's kinetic inductance, and difficult capacitive coupling to other systems. A suitable candidate easy to fabricate, resilient to applied

fields, and simple capacitive coupling is the lumped element resonator. Such type of resonator has already been used for some experiments that require magnetic fields [12], but a systematic study on the resonator's optimal geometry is yet to be undertaken. A lumped element resonator optimized for applied magnetic fields is therefore fundamental to pave the way towards better mesoscopic physics experiments under applied fields.

The energy losses in a superconducting resonator mainly stem from coupling to two-level systems (TLSs), from magnetic induced vortices, radiation, and at last quasiparticles originated from strayed IR light or microwave induced pair-breaking [6]. The first three of these loss mechanisms are known to be associated with the resonator geometry and therefore can be mitigated by optimizing the resonator design [6]. Two-level systems couple to the electric field and they are therefore dependent on the capacitance of the resonator. On the other hand vortex and radiation losses are known to be related to the inductance of the resonator, since it is where most current is located at resonance. Finally quasiparticle loss is attributed to the inductor, but its dependence on resonator geometry is yet unknown.

The outline of this thesis is as follows. To start, the theoretical framework will be presented. First we introduce the physics of superconductivity, from which we derive expressions describing crucial features for the design and understanding of our system. Secondly we focus on how to obtain lumped element components such as inductors and capacitors from a thin film superconducting pattern. We present the main figures of merit of resonators with exemplary derivations using circuit theory. Afterwards the work focuses on the design of our lumped element resonators and the approach used to simulate the resonator's response properties. We present the measurement setup used to characterize our resonators along with the method taken to perform the magnetic field alignment. Next we show transmission measurements of our resonators in a two-port network. We characterize the main loss forms and investigate its dependence on geometry by analyzing the power dependence of the resonators. Then we study how the in-plane and out-of-plane magnetic fields degrade the resonator's performance, focusing on the role of resonator geometry. Finally, the conclusions of this work will be presented, with a summary of this project and suggestions for future work following this research.



# Chapter 2

## Physics behind superconducting circuits

Our material consists of an interacting system of electrons, phonons and electromagnetic fields. In this chapter we introduce the theory of superconductivity to be able to derive an expression for the internal inductance of a microstrip inductor. First we give a brief overview of the properties of superconductors. Next we use the Drude model to understand conduction in normal metals. After that we find the conditions necessary to obtain infinite conductivity at DC and the first sign of kinetic inductance at AC, the former being a distinctive feature of superconductors. We complement the section by using the London analysis to predict the Meissner effect and the London penetration depth. We derive a simple expression for the kinetic inductance of a superconducting microstrip using the theory mentioned above. Then we introduce the microscopic theory of superconductivity, which allows us to derive a more accurate expression for the kinetic inductance. Finally we give expressions for the inductance and capacitance of a CPW, such that we can later calculate the proper dimensions of the transmission line probing the resonators making sure impedance matching is fulfilled. At last we provide a brief overview on the physics of the main loss forms in superconducting resonators.

### 2.1 Superconductivity

At reduced temperature the electrical resistance of all elemental metals decreases [13]. Nevertheless, Kamerlingh Onnes observed in 1911 that below some critical temperature  $T_c$  characteristic of the material, certain metals such as mercury, lead or tin had none DC electrical resistance and therefore became *perfect conductors*. A

new property of these materials was discovered in the year 1933 by Meissner and Ochsenfeld [14], *perfect diamagnetism*, the capability to expell almost completely magnetic field out of the material's bulk as it is cooled through  $T_c$ . The small distance the magnetic field can penetrate is known as the *penetration depth* ( $\lambda$ ). It was while analysing the behavior of the penetration depth that Abrikosov found in 1957 a distinction in the realm of superconducting materials. He classified as Type I superconductors those with a discontinuous breakdown of superconductivity in a first-order transition at  $H_c$ , whereas Type II superconductors showed a continuous increase in flux penetration starting at lower magnetic field  $H_{c1}$  up to a higher magnetic field  $H_{c2}$ . A key analysis of this fascinating result is the fact that flux penetrates in a regular array of flux tubes, each carrying a flux quantum  $\Phi_0$ . Each flux tube consists in a vortex of supercurrent that concentrates the flux towards the vortex center [13]. This leads to a non-perfect diamagnetism as well as a non-perfect conductivity when the Type II superconductor is in its intermediate state. Nevertheless, Type II superconductors offer technical advantages such as high critical temperatures ( $T_c$ ) and high critical magnetic fields. These practical benefits make Type II superconductors well suited for Superconducting Qubit applications.

## 2.2 Conductivity of normal metals

To be able to understand the peculiarities of superconducting materials, we first need to introduce the microscopic phenomena in normal metals underlying electrical conductivity. The non-perfect conductivity in normal metals stems from the electrons scattering off the ions in the lattice of the metal [15]. Such scattering decreases the kinetic energy of the electrons previously gained by the external electric field. Here we will use the Drude model to examine metallic conduction, since it allows to form a simple picture and gives rough estimates of properties with underlying complexity beyond the scope of this thesis.

We focus on the general case where the current is induced by a time-dependent AC electric field. This field can be expressed as

$$\mathbf{E}(r, t) = \Re\{\mathbf{E}(\omega)e^{-i\omega t}\} \quad (2.1)$$

In this case, applying classical mechanics to the electron motion we obtain [15]

$$\frac{d\mathbf{p}}{dt} = -\frac{\mathbf{p}}{\tau} - e\mathbf{E} \quad (2.2)$$

with  $\tau$  the phenomenological *relaxation time*, defined as the average time elapsed since the last electron's collision. We seek for  $\mathbf{p}$  to be of the form  $\mathbf{p}(t) = \Re\{\mathbf{p}(\omega)e^{-i\omega t}\}$ .

Substituting the expressions for  $\mathbf{p}(t)$  and  $\mathbf{E}(t)$  into Eqn. 2.2 and making sure the real and imaginary parts of the equation are fulfilled. We get to the following relation:

$$-i\omega \mathbf{p}(\omega) = -\frac{\mathbf{p}(\omega)}{\tau} - e\mathbf{E}(\omega) \quad (2.3)$$

Given that at any time  $t$  the average drift velocity of the electron  $\mathbf{v}$  is just  $\mathbf{p}(t)/m$ , with  $\mathbf{p}$  the total momentum per electron and  $m$  the effective electron mass, the current density is  $\mathbf{j} = -ne\mathbf{p}/m$  [15], where  $n$  is the number of conducting electrons per unit volume with velocity  $\mathbf{v}$ . Then using Eqn. 2.3 we obtain:

$$\mathbf{j}(t) = \Re\{\mathbf{j}(\omega)e^{-i\omega t}\} \rightarrow \mathbf{j}(\omega) = -\frac{n\mathbf{p}(\omega)}{m} = \frac{(ne^2)/m}{1/\tau - i\omega} \mathbf{E}(\omega) \quad (2.4)$$

This result can be written as  $\mathbf{j}(\omega) = \sigma(\omega)\mathbf{E}(\omega)$ , where  $\sigma(\omega)$  is known as the AC conductivity:

$$\sigma(\omega) = \frac{\sigma_0}{1 - i\omega\tau}, \sigma_0 = \frac{ne^2\tau}{m} \quad (2.5)$$

We can split Eqn. 2.5 into its real and imaginary part to get an easier expression to interpret:

$$\sigma(\omega) = \frac{ne^2\tau}{m(1 + \omega^2\tau^2)} + i\frac{ne^2\omega\tau^2}{m(1 + \omega^2\tau^2)} \quad (2.6)$$

The imaginary part of Eqn. 2.6 stems from the fact that under an applied AC field, the electrons do not respond instantaneously to the applied field. In fact, electrons gain momentum during the relaxation time  $\tau$ , then, when the applied field is reversed, the electrons first lose their momentum before changing their direction to the one of the new field.

Taking into account that at room temperatures the relaxation time  $\tau$  is typically of the order of  $10^{-14} - 10^{-15}s$  [15], then at microwave frequencies ( $\omega \sim 10^{10}$ ) we find  $\omega^2\tau^2 \ll 1$ , and therefore the imaginary term in Eqn. 2.6 is negligible.

## 2.3 Zero resistance and Meissner effect

We have seen in the previous section how the electrons scattering off the metallic ions in the lattice cause energy losses and a finite conductivity. If we consider a

non-scattering population of electrons  $n_s$ , this is we take the limit  $\tau \rightarrow \infty$  in Eqn. 2.6, we get:

$$\sigma(\omega)_{\tau \rightarrow \infty} \rightarrow i \frac{n_s e^2}{m\omega} \quad (2.7)$$

This result shows a complex impedance that, as we previously mentioned, is associated with the inertia of the (non-scattering) electron population  $n_s$  when the frequency-dependent applied electric field changes direction. Since the electron velocity is proportional to the current, the current lags the field just as it would in an inductor. Therefore Eqn. 2.7 represents the *kinetic inductance*. This concept will be further detailed in the following sections. It is straightforward to see that under an applied DC electric field ( $\omega = 0$ ) the conductivity goes to infinity accounting for the zero resistance of superconductors at DC.

Another unique property of superconductors besides being resistanceless at DC is the so-called Meissner effect, or as aforementioned, *perfect diamagnetism*. The latter was the first subject of study of F. London and H. London in 1935 [16]. Their goal was to examine in a quantitative way why a metal in its superconducting state expelled completely the magnetic field out of its bulk.

The London analysis starts with the two-fluid model proposed by Gorter and Casimir [17]. In such model there is one fraction of the total number of conduction electrons that contribute to the supercurrent at  $T < T_c$ . This quantity  $n_s$  is known as density of superconducting electrons and is temperature dependent. The remaining conducting electrons constitute the 'normal fluid' and therefore scatter as they would in a normal metal. These two population of conducting electrons in our metal can be considered to flow in parallel, since any small transitory electric field will induce the supercurrent of electrons  $n_s$  and fail to produce the 'normal' current. Hence we suppose a superconductor under an applied time-varying electric field. The classical equation of motion for the superconducting electrons can be obtained from Eqn. 2.2 in the limit  $\tau \rightarrow \infty$ . Taking into account that the current density carried by these electrons is  $\mathbf{j} = -en_s\mathbf{v}_s$  and using the adapted form of Eqn. 2.2 we obtain the first London equation:

$$\frac{d\mathbf{j}}{dt} = \frac{n_s e^2}{m} \mathbf{E} \quad (2.8)$$

Note that by taking the Fourier transform of the resulting equation we obtain the AC conductivity of the non-scattering electron gas obtained with the Drude model (Eqn. 2.7).

However, despite the First London equation (2.8) describing perfect conductivity, it does not explain how a superconductor is able to expel any magnetic flux density

from within its interior, the so-called *perfect diamagnetism* or *Meissner effect*. The application of Maxwell's equations to a perfect conductor describes diamagnetism of time-varying magnetic fields [15]. Nevertheless it is the set of constitutive conditions to Maxwell's equations suggested by the Londons that expel both DC and AC fields from the superconductor's bulk. The second London equation superconductors must obey reads:

$$\nabla \times \mathbf{j} = -\frac{n_s e^2}{mc} \mathbf{B} \quad (2.9)$$

Such restrictive London equation leads to the *Meissner effect*, caused by surface currents in the superconductor that screen out the applied field. Combining Eqn. 2.9 with the Ampere-Maxwell law allows to predict that currents and magnetic fields in superconductors mainly prevail within a layer of thickness  $\lambda_L$  from the surface, the so-called *penetration depth*. Such penetration depth in its ideal theoretical limit ( $T \rightarrow 0$ ) reads:

$$\lambda_L(0) = \left( \frac{mc^2}{4\pi n_s e^2} \right)^{1/2} \quad (2.10)$$

Its dependence on temperature is found empirically, and is approximately described by:

$$\lambda_L(T) \approx \lambda_L(0) \left[ 1 - \left( \frac{T}{T_c} \right)^4 \right]^{-1/2} \quad (2.11)$$

## 2.4 Internal inductance: Kinetic and magnetic

The kinetic inductance of superconducting electrons is the underlying phenomenon determining many macroscopic features, such as at what frequency does a lumped element resonator resonate. Therefore it is essential to obtain an accurate description of its behaviour. As previously mentioned, kinetic inductance is a result of charge carriers having mass, and therefore taking a certain finite time to respond to a time-varying external electric field. In this work we are interested in the kinetic inductance of a superconducting strip, therefore we will consider such particular case.

Let us assume a superconducting strip of thickness  $t$ , width  $W$  and length  $l$ , as illustrated in Figure 2.1 a). We recover Eqn. 2.4, obtained with the Drude model in the case of normal metals. Such expression in the superconducting limit  $\omega^2\tau^2 \gg 1$  can be rewritten as:

$$\mathbf{E}(\omega) = i\omega \frac{m}{ne^2} \mathbf{j}(\omega) \quad (2.12)$$

Thus, using the fundamental definition of voltage it yields:

$$V = \int \mathbf{E} \cdot d\mathbf{l} = \int i\omega \frac{m}{ne^2} \mathbf{j} \cdot d\mathbf{l} \quad (2.13)$$

In the case of superconducting strip thin films where the thickness of the strip is much smaller and the width much larger than the penetration depth, the current density across the film is uniform [18] and given by  $\mathbf{j} = I/Wt$ . Now the result for  $V$  becomes:

$$V = i\omega \frac{m}{ne^2} \frac{l}{Wt} I \quad (2.14)$$

From this result we can define the kinetic inductance  $L_k$  as:

$$V = i\omega L_k I \rightarrow L_k = \frac{m}{ne^2} \frac{l}{Wt} \quad (2.15)$$

It is straightforward then that the impedance reads

$$Z = \frac{V}{I} = i\omega L_k \quad (2.16)$$

which corresponds to an inductive behaviour with equivalent inductance  $L_k$ .

Nevertheless, kinetic inductance only accounts for one contribution to the total internal inductance of the material. The total internal inductance is the sum of the kinetic inductance ( $L_k$ ) and the magnetic inductance ( $L_m$ ). The latter is a result of the magnetic field energy density stored within the superconducting bulk created by the supercurrent [18]. It is defined as:

$$L_m = \frac{\Phi}{I} \rightarrow \Phi = L_m I \quad (2.17)$$

with  $I$  the current and  $\Phi$  its induced magnetic flux. Taking the derivative on both sides of the last expression and using Faraday's law we find:

$$V = L_m \frac{\partial I}{\partial t} + I \frac{\partial L_m}{\partial t} \approx L_m \frac{\partial I}{\partial t} \quad (2.18)$$

which showcases the inductive response of the magnetic inductance. The last approximation accounts for the fact that  $L_m$  is usually time-independent [19].

We can approximate the expression of the magnetic self-inductance of a strip by considering a long straight metal wire of length  $l$  and circular cross-section  $r$ , with

no ground plane or dielectric nearby. Following the derivation of [20], the magnetic inductance of such system reads:

$$L_m \approx \frac{\mu_0}{2\pi} l \left[ \ln \left( \frac{2l}{r} \right) - 1 \right] \quad (2.19)$$

with  $\mu_0 = 4\pi \cdot 10^{-7} \text{ H/m}$ . This expression indicates that for long and thin wires, the kinetic inductance will dominate over the small magnetic inductance. It must be noted that Eqn. 2.19 does not exactly represent the case of a micro/nanostrip on top of a dielectric layer, however the typical geometries of our inductors yield lower  $L_m$  values than Eqn. 2.19, hence it serves the purpose of showing that  $L_T = L_k + L_m \approx L_k$  [19].

Note than in a normal metal the kinetic inductance is very small compared to the resistive nature of the material, since usually  $\omega\tau \ll 1$  and only  $\omega\tau \geq 1$  at very high frequencies. However, the resistive part in a superconducting strips goes to zero for temperatures far below  $T_c$ . Causing the superconducting strip to behave as an inductor with effective inductance  $L_k$ .

A more accurate description of the kinetic inductance in superconductors requires the introduction of the microscopic theory of superconductivity.

## 2.5 Microscopic theory of superconductivity

The next step in understanding the phenomenon of superconductivity relies on the key theory proposed by Bardeen, Cooper, and Schrieffer in 1957 [21]. In such theory it is shown how an attractive interaction lead by phonon-electron interaction is able to form bound pairs of electrons occupying states with equal and opposite momenta and spin. These are the so-called Cooper pairs. The keystone to the formation of Cooper pairs is the motion of the ion cores of the material. When an electron is introduced in the lattice, it attracts the near positive ions, which in turn attract a second electron producing this way an effective attractive interaction between the electrons. If this attractive interaction exceeds the repulsive screened Coulomb interaction, then a Cooper pair is formed. The breaking of a Cooper pair produces two individual unpaired electrons, and the minimum energy to break a Cooper pair was one of the crucial predictions by this theory, this energy is  $E_g(T) = 2\Delta(T)$ . The quantity  $\Delta$  was predicted to be temperature-dependent, going from zero at  $T_c$  to a certain saturation value  $E_g(0)$  for  $T \ll T_c$ . Eventually gap widths measurements proved the prediction right [13] and therefore the microscopic theory valid, making this way the BCS theory the cornerstone of superconductivity.

### 2.5.1 Kinetic inductance from BCS theory

Consequently, to obtain a proper expression for  $L_k$  in a superconductor we must replace with the Cooper pair mass ( $m \rightarrow 2m_e$ ), the Cooper pair charge ( $e \rightarrow 2e$ ), and the Cooper pair density  $n_s$  in Eqn. 2.15:

$$L_k = \frac{m_e}{2n_s e^2} \frac{l}{Wt} \quad (2.20)$$

where the Cooper pair density depends on temperature as  $n_s(T) = n_s(0)(1 - T/T_c)$  and current (for this work we consider currents far below the pair-breaking current). This equation only holds for temperatures close to  $T_c$  and small currents [22]. To obtain an equation for  $L_k$  valid for all  $T$  we can use the BCS theory. We start by assuming the low-frequency limit, this is  $\hbar\omega \ll 2\Delta$ . In this limit Mattis-Bardeen derived the formula for the complex conductivity expressed as a ratio of the imaginary conductivity ( $\sigma_i$ ) to the normal state conductivity ( $\sigma_n$ ) [13] as:

$$\frac{\sigma_i}{\sigma_n} = \frac{\pi\Delta}{\hbar\omega} \tanh\left(\frac{\Delta}{2k_B T}\right) \quad (2.21)$$

As we saw in Section 2.4, the AC conductivity relates the current density and the applied electric field as  $\mathbf{j}(\omega) = \sigma(\omega)\mathbf{E}(\omega)$ . Then, by using the definition of voltage and considering a uniform current density we can obtain the impedance:

$$V = \int \mathbf{E} \cdot d\mathbf{l} = \int \frac{1}{\sigma} \mathbf{j} \cdot d\mathbf{l} = \frac{l}{\sigma W t} I \quad (2.22)$$

We can split the conductivity into its real and imaginary parts as  $\sigma = \sigma_r - i\sigma_i$ . For the following we assume  $\sigma_i \gg \sigma_r$ , as it is the case in superconductors [13]. Then the impedance reads:

$$Z = \frac{V}{I} = \frac{l}{W t} \frac{1}{\sigma_r - i\sigma_i} \approx \frac{l}{W t} \left[ \frac{\sigma_r}{\sigma_r} + \frac{i}{\sigma_i} \right] = R + Z_L(\omega) \quad (2.23)$$

Recall the complex impedance is associated to the kinetic inductance as  $Z_L(\omega) = i\omega L_k$  [23]. Combining that with Eqn. 2.21 and using the definition for sheet resistance as  $R_{sq} = (t\sigma_n)^{-1}$  we obtain the temperature dependent expression for the kinetic inductance in the low frequency regime [22]:

$$L_k = \frac{l}{W} \frac{R_{sq} h}{2\pi^2 \Delta} \frac{1}{\tanh\left(\frac{\Delta}{2k_B T}\right)} \quad (2.24)$$

We can take a step further and simplify Eqn. 2.24 for  $T \ll T_c$ , which will be the operating range in this work. In this limit it is known that  $\Delta \approx 1.76k_B T_c$  [13], therefore the kinetic inductance per square reads:

$$L_k \approx \frac{R_{sq}h}{2\pi^2 1.76 k_B T_c} \quad (2.25)$$

This equation is important to understand how the resonance frequency depends on the kinetic inductance at  $T \ll T_c$  and for small changes in frequency. In particular, in this work we will apply in plane and out of plane magnetic fields, which will break Cooper pairs as they increase (specifically in the inductor's superconducting strip), and hence increase the kinetic inductance (c.f. Eqn. 2.20), and therefore decrease the resonance frequency of the LE resonator (see in Section 3.1.2 how a microstrip models an inductor).

## 2.6 Kinetic and magnetic inductance of CPW

Deriving the kinetic inductance for a superconducting microstrip is essential for understanding the behaviour of LE resonators under applied fields. Nevertheless the transmission line probing the resonator has the geometry of a Coplanar Waveguide (c.f. 2.1 b)). As we will see in Section 3.1.1, the characteristic impedance of the line is  $Z_0 = \sqrt{L/C}$  and is chosen to be  $50\Omega$  due to impedance matching. Therefore it is necessary to design the transmission line such that  $Z_0 = 50\Omega$ . Since the inductance of a superconducting coplanar waveguide is kinetic and magnetic we need an expression for  $L$  and  $C$  depending on the geometry of the feedline.

In the case where the center electrode is much smaller than the wavelength of the operating signal, a quasi-TEM mode can propagate in the CPW. Assuming that the film thickness is smaller than the depth of the current flow  $\lambda_L$  so that the current distribution is uniform, the magnetic and kinetic inductance per unit length are given by [24]

$$L_m = \frac{\mu_0}{4} \frac{K(k')}{K(k)} \quad (2.26)$$

$$L_k = \mu_0 \frac{\lambda_L^2}{Wt} g(s, W, t) \quad (2.27)$$

which is obtained through the conformal mapping technique. Note that  $K(k)$  is the complete elliptic integral of the first kind with modulus  $k = W/(W + 2s)$ ,  $k' = (1 - k^2)^{1/2}$ . Moreover,  $g(s, W, t)$  is a geometrical factor depending on the center conductor's width  $W$ , the film thickness  $t$  and lastly the spacing between the center

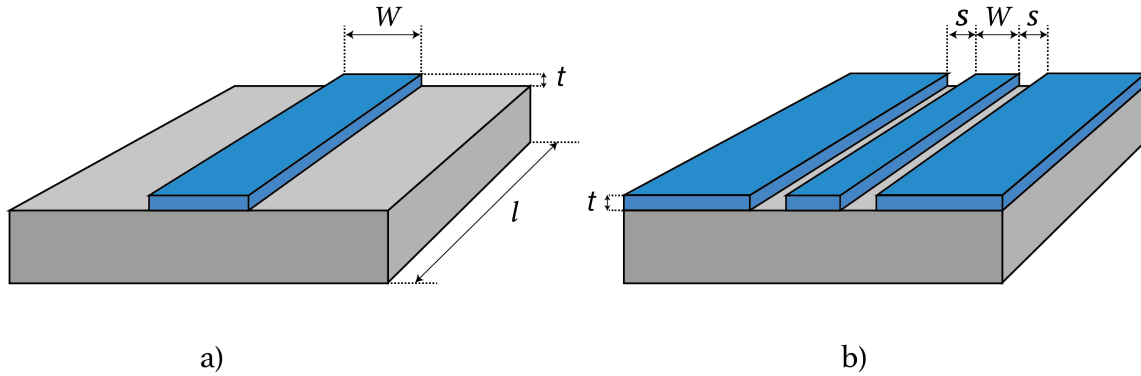


Figure 2.1: a) Microstrip of width  $W$ , length  $l$  and thickness  $t$  (not to scale). b) Coplanar Waveguide (CPW) of center conductor width  $W$ , thickness  $t$  and spacing between center conductor and ground planes  $s$  (not to scale).

conductor and the ground planes  $s$ . It is weakly dependent on  $t$  and  $s$  and shows that the kinetic inductance decrease with decreasing  $t$  and  $W$  [25].

On the other hand, the capacitance per unit length obtained using conformal mapping techniques is given by [26]

$$C = 4\epsilon_0\epsilon_{eff} \frac{K(k)}{K(k')} \quad (2.28)$$

where  $C$  depends not only on the geometry but also on the effective dielectric constant of the substrate  $\epsilon_{eff}$ .

## 2.7 Material losses in superconducting resonators

Here we provide an overview for loss channels in superconducting resonators. We describe two-level systems, magnetic vortices, radiation and quasiparticle dissipation.

### 2.7.1 Two-level systems loss

In amorphous materials (non-crystalline lattice), the randomness of the atomic arrangements origin two-level defects (TLS) within the material at low temperatures [27]. These TLS have low energy and consequently saturate at high temperatures. Nonetheless at low temperatures they can dominate certain properties of the material. The underlying microscopic physics of these defects is still unclear [28], but the main line of thought is that some atoms can tunnel between two sites of the

amorphous solid, resulting in two possible quantum states. This is the so-called Standard Tunneling Model (STM) [29]. One TLS can diminish the performance of a resonator by absorbing a photon from the resonator and then relaxing by emitting a phonon into the material [30]. Moreover TLS can slightly change the dielectric constant of the material and induce excess phase noise to the resonators [31]. Even if our system does not contain a dielectric, it was shown [32] that TLS on surfaces and interfaces of the superconductor and crystalline Si substrate can be a relevant loss form. The intrinsic TLS loss is governed by the density and electric dipole moment of the tunneling states in the material, therefore it can couple to the electric field of the resonator. For that reason TLS loss is attributed to the capacitor of the resonator, and is therefore correlated with its geometry.

### **2.7.2 Magnetic vortices loss**

Magnetic flux can be trapped in the material in the form of tubes with normal metal core. In the presence of current the Lorentz force make the flux tubes move sideways [13]. When the flux tubes are pinned in impurities of the material, a finite current must be reached to overcome the Lorentz force. The movement of flux tubes (in particular their non-superconducting core) induce a resistive voltage, which, when being near the resonator, lowers its quality factor. Therefore vortex losses is associated with the current flowing through the resonator. Since at resonance most current is localized at the inductor (c.f. Fig. 4.3), it is the inductive component the main source of vortex-induced losses. This loss form is then correlated with the geometry of the inductor, as it has been established in previous research [33].

### **2.7.3 Quasiparticles loss**

Quasiparticle loss may be induced by different physical phenomena: i) thermal quasiparticle loss, ii) quasiparticle loss due to stray IR light and iii) quasiparticle loss due to microwave induced cooper pair breaking. The first is almost negligible at the low temperature regime, while the second one can be addressed with proper shielding from the environment. The third type however, stems from the essential microwave tone used to probe the resonator. Even when the microwave photons used for read out have very small energy compared to the superconductor gap ( $\hbar\omega \ll 2\Delta$ ), they can be absorbed by quasiparticles above the energy gap  $E \geq \Delta$ . This energy gain scatters the quasiparticle to a higher energy level. When eventually it relaxes back to an energy level slightly above the gap, it emits a pair-breaking phonon, which produce more quasiparticles. This multiplication process is supported by theoretical studies [34] and experimental observations [35]. It is well known too that both the

quality factor and resonance frequency decrease with increasing microwave power as a result of the creation of excess quasiparticles from microwave absorption. However, it is yet unclear the dependence of this loss on geometry. A recent approach to diminish the negative effect of quasiparticles consists in finding ways of evacuating them from the relevant parts of the device. A promising method of this kind is gap engineering [36], which involves adding regions in the device with subgap states so that quasiparticles can relax in them.

#### 2.7.4 Radiation loss

Resonators can lose their energy in the form of radiation into free space. This way loops of electrical current may be induced by a varying magnetic field in the conductive material on the backside of the substrate [37]. These currents are known as Eddy currents. Studies on the effect of backside coating the chip with different conductive media show that using thick substrates or high conductive materials on the backside of the substrate mitigate radiative loss [37]. This loss has been shown to be geometry correlated and power independent [38].

#### 2.7.5 Loss uncertainty

Despite being able to design, fabricate, and measure superconducting microwave resonators in a systematic way, resonator loss can vary from resonator to resonator (besides being identical) [39] in the same chip exposed to the same fabricating conditions. The range of  $Q_c$  for the same resonator located in different places of the same chip can vary more than an order of magnitude. This deviation is thought to stem from slight changes in the microwave setup. On the other hand the internal quality factor ( $Q_i$ ) can vary up to an order of magnitude, both at low and high powers, which suggests that fabrication processes still need to be optimized to completely avoid resonator mismatch. In fact, different quality factors have been observed for the same resonator over different cooldowns [40] and even over time [41]. Therefore the extracted quality factors of a particular resonator has an associated uncertainty of up to one order of magnitude.

# Chapter 3

## Engineering behind microwave circuits

### 3.1 Lumped elements in microwave circuits

Under certain conditions for alternating signal frequency and electrical circuit size we can make the lumped-element simplification. When the circuit size is significantly smaller than the signal wavelength, the voltage and current through any of the electrical components do not vary with position but only in time [42]. Therefore, in the field of microwave circuits, components such as inductors or capacitors can be described as lumped or quasi-lumped elements. This not only entails advantages in terms of modelling and circuit design but also smaller interaction effects between circuit elements [43]. In this section we introduce their physical description and highlight their main properties.

#### 3.1.1 Lumped-element circuit model for a transmission line

Transmission lines are a fundamental element in microwave circuits, as their goal is to carry alternating currents in a contained manner. In the field of superconducting circuits it is practical to fabricate transmission lines in the form of coplanar waveguides. As previously mentioned, in circuit theory the physical dimensions of the system are much smaller than the signal wavelength, however, transmission lines might be comparable to the size of a wavelength, and therefore voltages and currents can vary in magnitude and phase over the lines length.

Since transmission lines for transverse electromagnetic (TEM) wave propagation have at least two conductors, is common to schematically illustrate a transmission line as a two-wire line (c.f. Fig. 3.1 a)). A small section of the transmission line

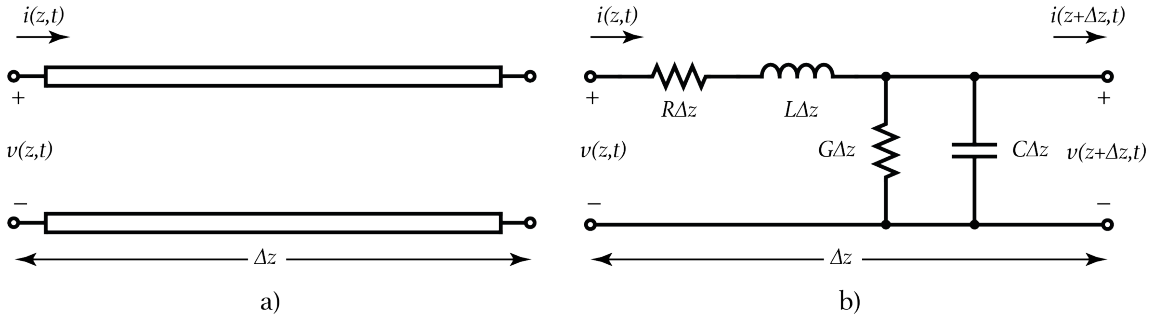


Figure 3.1: a) Schematic of a piece of a transmission line. b) Lumped-element equivalent.

can be modeled as a lumped-element circuit and the whole transmission line becomes an array of such small sections (c.f. Fig. 3.1 b)). This piece of line has infinitesimal length  $\Delta z$ , R resistance for both conductors per unit length (in  $\Omega/m$ ), L self-inductance for both conductors per unit length (in  $H/m$ ), G shunt conductance due to dielectric loss per unit length (in  $S/m$ ) and finally C the shunt capacitance per unit length (in  $F/m$ ) due to the short distance between both conductors.

Using the lumped element model in Figure 3.1 b) and Kirchoff's voltage and current laws we obtain

$$v(z,t) - R\Delta z i(z,t) - L\Delta z \frac{\partial i(z,t)}{\partial t} = v(z + \Delta z, t) \quad (3.1)$$

$$i(z,t) - G\Delta z v(z,t) - C\Delta z \frac{\partial v(z + \Delta z, t)}{\partial t} = i(z + \Delta z, t) \quad (3.2)$$

Since our focus lies on superconducting materials we look at the particular case where losses  $R, G$  are very small, hence  $R, G \sim 0$ . We divide the expressions by  $\Delta z$  and take the limit  $\Delta z \rightarrow 0$  so that we can approximate the fractions by spatial derivatives. It results in the following differential equations:

$$\frac{\partial v(z,t)}{\partial z} = -L \frac{\partial i(z,t)}{\partial t} \quad (3.3)$$

$$\frac{\partial i(z,t)}{\partial z} = -C \frac{\partial v(z + \Delta z, t)}{\partial t} \quad (3.4)$$

This set of differential equations is well known as the *Telegrapher equations* since they were originally developed to describe telegraph wires. These equations are the starting point for characterizing  $V(z), I(z)$  wave propagation along the transmission

line (in our case lossless). By considering a harmonic steady-state excitation of the form  $V(z) = \Re\{V(z)e^{j\omega t}\}, I(z) = \Re\{I(z)e^{j\omega t}\}$  the previous expressions simplify to

$$\frac{\partial V(z)}{\partial z} = -j\omega L I(z) \quad (3.5)$$

$$\frac{\partial I(z)}{\partial z} = -j\omega C V(z) \quad (3.6)$$

with  $j = \sqrt{-1}$  the imaginary unit. These equations may be combined by taking their spatial derivative to form two wave equations, for  $V(z)$  and  $I(z)$ :

$$\frac{\partial^2 V(z)}{\partial z^2} - \gamma^2 V(z) = 0 \quad (3.7)$$

$$\frac{\partial^2 I(z)}{\partial z^2} - \gamma^2 I(z) = 0 \quad (3.8)$$

where  $\gamma = j\omega\sqrt{LC}$  is the so-called complex propagation constant. The solutions to the wave equations are known to be

$$V(z) = V_0^+ e^{-\gamma z} + V_0^- e^{\gamma z} \quad (3.9)$$

$$I(z) = \frac{V_0^+}{Z_0} + e^{-\gamma z} - \frac{V_0^-}{Z_0} e^{\gamma z} \quad (3.10)$$

with  $V_0^+, V_0^-$  arbitrary constants of integration, which are determined by two boundary conditions. There  $Z_0 = \sqrt{L/C}$  is the characteristic impedance of the line, which is usually chosen to be  $50\Omega$  for impedance matching reasons. The wavelength on the line is  $\lambda = \frac{2\pi}{\omega\sqrt{LC}}$  and the phase velocity is  $v_p = \frac{1}{\sqrt{LC}}$ .

### 3.1.2 Design of microwave lumped elements

The design of the main lumped element components such as capacitors, inductors and resistors at microwave frequencies is based on short TEM lines like microstrip lines [43], always smaller than the operating wavelength. Lumped elements can be used in microwave circuits at frequencies up to 60 GHz if they satisfy the condition  $l < \lambda/10$  [42], this is their size is much smaller than the operating wavelength. To be able to understand how to build such components using transmission lines we first need to look at the generic case of a line with length  $l$  terminated with an impedance  $Z_L$ .

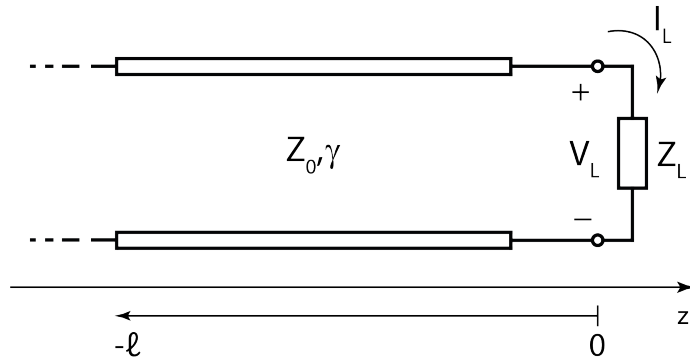


Figure 3.2: Transmission line terminated with an arbitrary load  $Z_L$ .

### The Terminated lossless line

Figure 3.2 shows a lossless transmission line of length  $l$  terminated with a load impedance  $Z_L$ . In the previous section we found the total voltage and current on the line to be Eqn. 3.9, Eqn. 3.10 respectively. In order to study the effect of the load impedance on the wave propagation, we use the relation between the total voltage and current at  $z = 0$ :

$$Z_L = \frac{V(0)}{I(0)} = \frac{V_0^+ + V_0^-}{V_0^+ - V_0^-} Z_0 \quad (3.11)$$

Solving Eqn. 3.11 for  $V_0^+$  we can obtain the voltage reflection coefficient  $\Gamma$  as a function the impedances of the system:

$$\Gamma = \frac{V_0^-}{V_0^+} = \frac{Z_L - Z_0}{Z_L + Z_0} \quad (3.12)$$

It must be noted that the impedance seen looking into the line varies with position. For instance at a distance  $z = -l$  from the load, the input impedance reads

$$Z_{in} = \frac{V(-l)}{I(-l)} = \frac{V_0^+(e^{\gamma l} + \Gamma e^{-\gamma l})}{V_0^+(e^{\gamma l} - \Gamma e^{-\gamma l})} Z_0 \quad (3.13)$$

Using Eqn. 3.12 for  $\Gamma$  in Eqn. 3.13 we end up with

$$Z_{in} = \frac{(Z_L + Z_0)e^{\gamma l} + (Z_L - Z_0)e^{-\gamma l}}{(Z_L + Z_0)e^{\gamma l} - (Z_L - Z_0)e^{-\gamma l}} Z_0 = \frac{Z_L \cosh \gamma l + Z_0 \sinh \gamma l}{Z_0 \cosh \gamma l + Z_L \sinh \gamma l} Z_0 \quad (3.14)$$

This result is the building block from which we can obtain lumped elements such as capacitors, inductors and resistors by choosing the proper load.

### Capacitor

To start with, an ideal capacitor of capacitance  $C$  is able to store and release electric energy  $W_E$  without dissipating any power [43]. Its capacitance is defined as  $C = Q(t)/V(t)$  with  $Q(t)$  the charge in each conductor and  $V(t)$  the voltage between them. Combining the definition of  $C$  with the fact that current is the time derivative of the charge  $Q(t)$  we come up with an expression relating current and voltage:

$$i(t) = C \frac{\partial V}{\partial t} \rightarrow i(\omega) = j\omega Cv(\omega) \quad (3.15)$$

From which we can extract the impedance of a capacitor for a certain frequency  $\omega$ :

$$Z_{Cap} = \frac{1}{j\omega C} \quad (3.16)$$

It is possible to get the same result when considering lossless transmission line terminated with an infinite load impedance, in other words, an open circuit. Taking Eqn. 3.13 in the limit  $Z_L \rightarrow \infty$  we get

$$Z_{in} \approx \frac{Z_0}{\tanh \gamma l} \approx \frac{Z_0}{\gamma l - \frac{1}{3}(\gamma l)^3 + \dots} \quad (3.17)$$

Therefore, when  $\gamma l \ll 1$  we may take the Taylor expansion ( $\frac{1}{x-ax^3} \approx x + ax + \dots$ ) to obtain

$$Z_{in} \approx \frac{Z_0}{\gamma l} + \frac{Z_0 \gamma l}{3} \quad (3.18)$$

For a lossy transmission line [42]

$$\gamma = \sqrt{(R^* + j\omega L^*)(G^* + j\omega C^*)} \quad \text{and} \quad Z_0 = \sqrt{\frac{R^* + j\omega L^*}{G^* + j\omega C^*}} \quad (3.19)$$

being  $R^*, L^*$ ,  $G^*$ , and  $C^*$  per-unit-length quantities previously defined in Section 3.1.1. We get to a final expression by combining Eqn. 3.19 with Eqn. 3.18 in the limit  $G^* \ll \omega C^*$ :

$$Z_{in} \approx \frac{G^*}{l(\omega C^*)^2} + \frac{R^* l}{3} + \frac{1}{l j \omega C^*} + \frac{j \omega L^* l}{3} \quad (3.20)$$

Finally, we can use the total quantities to get:

$$Z_{in} \approx \frac{G}{(\omega C)^2} + \frac{R}{3} + \frac{1}{j\omega C} + \frac{j\omega L}{3} \quad (3.21)$$

being  $R$ ,  $G$ ,  $L$  and  $C$  the total quantities with respect to the transmission line. This result entails that in the case where the transmission line is made out of superconducting material (i.e.  $R, G \approx 0$ ) then the transmission line behaves as a lumped element capacitor with capacitance  $C$  plus an inductive parasitic contribution. For right dimensions of the transmission line the parasitic inductive contribution is very small and can be neglected, resulting then in a transmission line that behaves as a lumped capacitor with capacitance  $C$  (c.f. Figure 3.3 a)).

## Inductor

An inductor of inductance  $L$  is capable of storing and releasing magnetic energy  $W_m$  while, ideally, not dissipating any power nor storing electric energy. Its inductance is defined as  $L = \Phi_B/I$ , with  $I$  the current through the conductor and  $\Phi_B$  the magnetic flux generated by that given current. The change in flux created by the change in current induces a voltage across the inductor, hence, using Faraday's law of induction one can extract the mathematical description of an inductor:

$$v(t) = L \frac{\partial i(t)}{\partial t} \rightarrow v(\omega) = j\omega L i(\omega) \quad (3.22)$$

From which we can obtain the impedance of an inductor for a certain frequency  $\omega$ :

$$Z_{ind} = j\omega L \quad (3.23)$$

Now let us show how a transmission line terminated with a zero impedance load (i.e. a short-circuit) is able to reproduce the same behavior. We take Eqn. 3.13 in the limit  $Z_L \rightarrow 0$  and focus on a small piece of transmission line ( $\gamma l \ll 1$ ):

$$Z_{ind} \approx Z_0 \tanh \gamma l \approx Z_0 (\gamma l - \frac{1}{3}(\gamma l)^3 + \dots) \approx R + j\omega L \quad (3.24)$$

with  $R$ ,  $L$  the total resistance and inductance of the transmission line. Hence a short-circuited short transmission line behaves like a resistor in series with an inductor, however, in the case of a superconducting material ( $R \approx 0$ ) the system is equivalent to a lumped inductor with inductance  $L$  (c.f. Figure 3.3 b)).

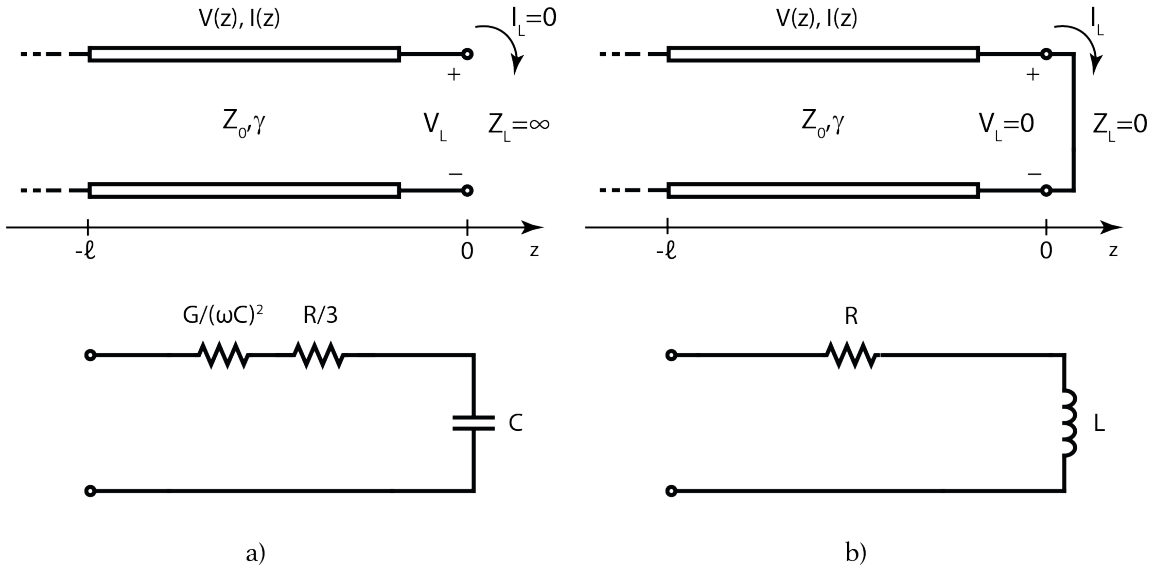


Figure 3.3: a) Transmission line of length  $l$  terminated with a load impedance  $Z_L = \infty$  (open circuit) and its equivalent circuit at the bottom. b) Transmission line of length  $l$  terminated with a load impedance  $Z_L = 0$  and its equivalent circuit at the bottom.

### Non ideal lumped elements

Special cases of transmission lines terminated with specific load lead to either lumped capacitors or lumped inductors. Nonetheless we have seen that there are some parasitic contributions not desired for their ideal performance. Using a superconducting material is the first step to having actual lumped elements, since losses are minimized. When it comes to the parasitic inductive contribution found in Eqn. 3.21 we must check that it does not dominates the transmission line behavior. The parasitic contribution stems from the capacitor's finite size [43] and therefore may be treated as a parasitic inductor in series with the ideal capacitor, as shown in Figure 3.4 a). The overall impedance of such system can be written as:

$$Z_{C_p} = \frac{1}{j\omega C} + j\omega L_p = \frac{1}{j\omega C}(1 - \omega^2 L_p C) = \frac{1}{j\omega C_p} \quad (3.25)$$

Equation 3.25 indicates that the ideal-parasitic circuit can be modeled as a capacitor with an effective capacitance  $C_p$  that can be expressed as

$$C_p = \frac{C}{1 - \omega^2 L_p C} = \frac{C}{1 - (\omega/\omega_p)^2} \quad (3.26)$$

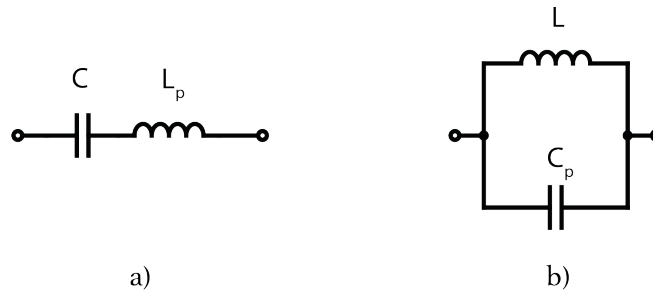


Figure 3.4: a) Ideal capacitor in series with parasitic inductor. b) Ideal inductor in parallel with parasitic capacitor.

where  $\omega_p = 1/\sqrt{L_p C}$  is defined as the capacitor's self-resonance frequency. In order for the capacitor to behave ideally one has to operate at frequencies lower than  $\omega_p$ , where  $C_p \approx C$  is fulfilled.

On another note, inductor conductor lines are usually shaped forming multiple meanders to minimize chip footprint. This geometry allows two conductors that carry current to be in close proximity, therefore making their magnetic flux lines overlap and interact with each other. Specially if the currents flow in opposite directions, then the inductance in each conductor decreases, this effect is the so-called *mutual inductance*. It must also be taken into account the parasitic capacitance that arises from the interturns of the inductor. Such parasitic capacitance ( $C_p$ ) is modeled as a capacitor in parallel with the ideal inductor, as illustrated in Figure 3.4 b). The impedance of the  $LC_p$  circuit is:

$$Z_{L_p} = \left( \frac{1}{j\omega L} + \frac{1}{1/j\omega C_p} \right)^{-1} = \frac{j\omega L}{1 - \omega^2 LC_p} = j\omega L_p \quad (3.27)$$

As seen in Eqn. 3.27 the  $LC_p$  system can be thought of as an ideal inductor with effective inductance  $L_p$ . Such inductance reads

$$L_p = \frac{L}{1 - \omega^2 LC_p} = \frac{L}{1 - (\omega/\omega_p)^2} \quad (3.28)$$

where we used  $\omega_p = 1/\sqrt{LC_p}$  defined as the self-resonance frequency of the inductor. At frequencies lower than  $\omega_p$  the inductor will behave almost ideally ( $L_p \approx L$ ), however, at frequencies near the self-resonant frequency the capacitor contribution leads to larger values of the inductance ( $L_p \gg L$ ). Past the self-resonance frequency the inductor behaves capacitively.

## 3.2 Modelling of Resonator circuits

The design and characterization of microwave superconducting resonators require a circuit model that best describes its system. Using electrical circuit theory one can find such model and the key effective parameters that describe the microwave components. In this section we construct a basic equivalent-circuit model for a single resonator coupled to a feedline and extract the basic parameters that describe our lumped-element microwave resonator.

### 3.2.1 Circuit model

Microwave resonators can usually be modeled by RLC lumped-element resonators at frequencies near resonance. In the following sections we will show how an inductor in parallel with a capacitor behaves like a resonator, and how such resonator can couple to the external environment in order to be measured.

### 3.2.2 Unloaded parallel RLC circuit

The lumped element resonator studied in this work can be described by the classic parallel RLC resonator. This system comprises a capacitor, inductor, and resistance in parallel, the lumped element components described in Section 3.1.2. To start with, we consider an unloaded resonator disconnected from the outside world as illustrated in Figure 3.5 a). The figures of merit used to define the resonator are its *resonance frequency*  $f_r$  and its *quality factor*  $Q$ .

When an inductor is connected in parallel with a capacitor, the current and voltages in the circuit oscillate between the inductor and the capacitor. The frequency of this oscillations is the so-called resonance frequency, and it depends on the values of inductance and capacitance of the elements in the circuit. When an AC voltage source with the same frequency as the characteristic LC oscillations is connected to the parallel LC circuit, then, from the perspective of the voltage source the LC combination behaves like an open circuit. In other words, when the average magnetic energy stored in the inductor is the same as the average electric energy stored in the capacitor then resonance occurs [42]:

$$W_e = \frac{1}{4}|V|^2C = \frac{1}{4}|V|^2\frac{1}{\omega^2L} = W_m \rightarrow \omega_0 = \frac{1}{\sqrt{LC}} \quad (3.29)$$

Therefore  $\omega_0$  is defined as the resonance frequency. It must be noted that at this

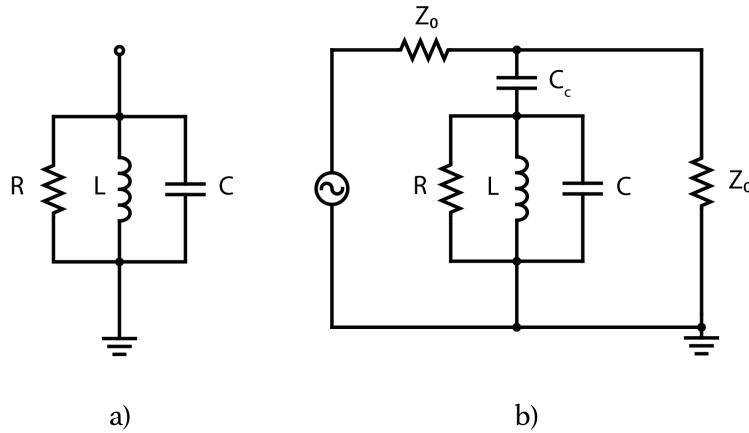


Figure 3.5: a) Unloaded parallel RLC resonator. b) RLC resonator capacitively coupled to a feedline.

frequency the input impedance of the RLC system is purely real:

$$Z_{in}(\omega) = \left( \frac{1}{R} + \frac{1}{j\omega L} + j\omega C \right)^{-1} \rightarrow Z_{in}(\omega_0) = R \quad (3.30)$$

The most fundamental description for the quality factor is:

$$Q = \omega \frac{\text{energy stored}}{\text{average power dissipated}} \quad (3.31)$$

This quantity represents the loss of the circuit, which may account for any of the losses mentioned in Section 2.7. Such losses are modeled by an effective resistance \$R\$ in the equivalent circuit (the lower the internal losses the higher the effective \$R\$). Thus, the average power dissipated in the circuit is:

$$P_{loss} = \frac{1}{2} \frac{|V|^2}{R} \quad (3.32)$$

Taking into account that at resonance \$W\_m = W\_e\$, we find the unloaded \$Q\$ to be:

$$Q_i = \omega_0 \frac{W_m + W_e}{P_{loss}} = \omega_0 RC = \frac{R}{\omega_0 L} \quad (3.33)$$

From now on this quality factor due to internal losses will be referred to as internal quality factor.

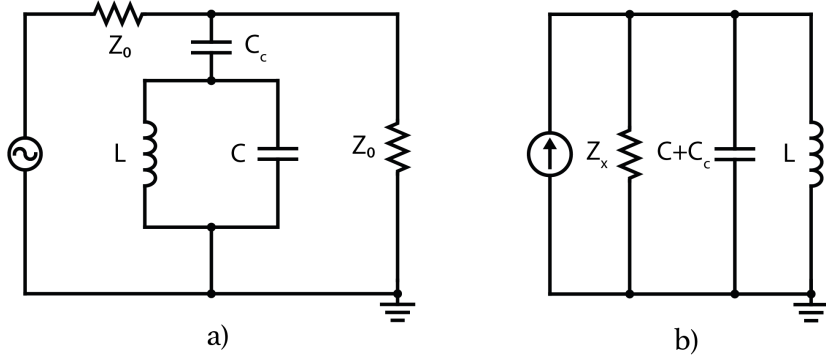


Figure 3.6: Capacitive coupling a) to an environment of impedance  $Z_0$  through a capacitor  $C_c$ . b) Effective equivalent circuit in the limit  $\omega C_c \ll Z_0$ .

### 3.2.3 Loaded parallel RLC circuit

In the real world, however, the resonator is probed by additional circuitry, which introduces additional loss and hence lowers the overall  $Q$ , now denoted  $Q_T$ . The coupling ( $Q_c$ ) and internal ( $Q_i$ ) quality factor add up in the following way:

$$\frac{1}{Q_T} = \frac{1}{Q_c} + \frac{1}{Q_i} \quad (3.34)$$

In this work the parallel RLC resonator is coupled to a feedline through a coupling capacitance  $C_c$  as illustrated in Figure 3.5 b). To see how this coupling affects the RLC resonator we find an expression for  $Q_c$  in the regime  $\omega C_c Z_0 \ll 1$ ,  $\omega C_c Z_x \gg 1$ , the derivation can be found in appendix A. Note that this assumptions are fulfilled at our operating regime, where  $\omega \sim 10^{10}$  rad/s,  $Z_0 \approx 50 \Omega$ ,  $C_c \sim 10^{-14}$  F and thus  $\omega C_c Z_0 \sim 10^{-3} \ll 1$ . The final expression describing the coupling quality factor reads:

$$Q_c = \omega_0 C_T Z_x = \sqrt{\frac{C_T}{L}} \frac{2}{\omega_0^2 C_c^2 Z_0} \quad (3.35)$$

with  $C_T = C + C_c$  the total capacitance,  $\omega_0 = 1/\sqrt{LC_T}$  the resonance frequency and  $Z_0$  the impedance of the input/output lines.

Thus by coupling the resonator capacitively to probing circuitry we add an effective capacitance  $C_c$  which will shift the resonance frequency, and an effective parallel resistance  $Z_x$  which ultimately will change the overall  $Q_T$ .

Equation 3.35 gives insight into the main parameters governing  $Q_c$ . The capacitive element linking the resonator to the feedline is essential in the design of the

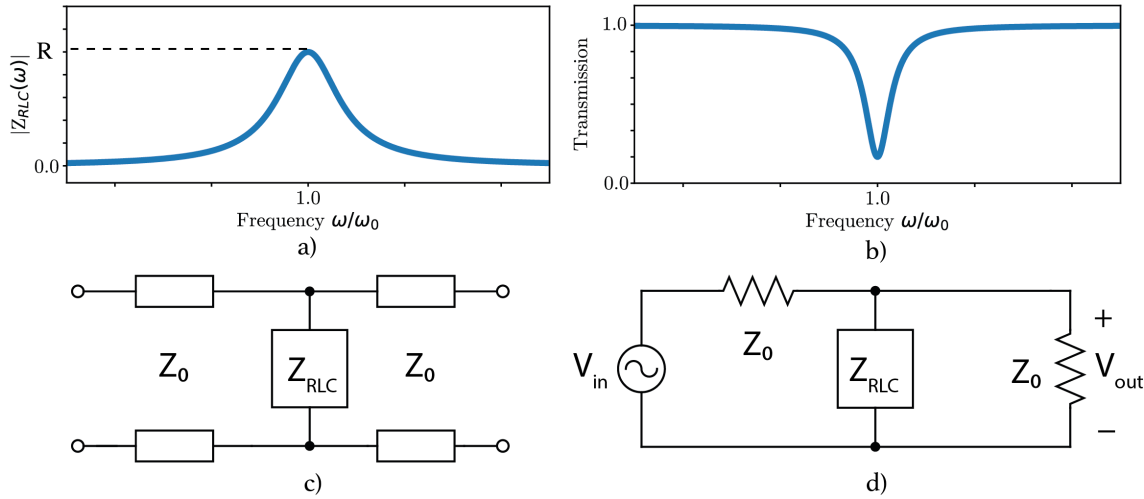


Figure 3.7: a) Impedance of the RLC parallel resonator. b) Transmission of the RLC resonator. c) Network representation of a resonator. d) Equivalent circuit of the resonator in the two-port system.

whole system, since in the regime  $Q_c \ll Q_i$  the coupling dominates the signal shape and the accuracy of measured  $Q_i$  is lower [6]. While for  $Q_c \gg Q_i$  the signal is reduced and it is harder to measure [1].

### 3.2.4 Transmission of a parallel RLC resonator

To be able to measure the resonator response and extract its resonance frequency and quality factors the two-port technique is used (transmission measurement). Figures 3.7 c),d) show a parallel RLC resonator coupled to a transmission line of characteristic impedance  $Z_0$  forming a two-port network. Minimum transmission occurs at resonance since the impedance of the parallel resonator is maximum at resonance, see Figure 3.7 a). Recall that for the effective  $R$  modelling the internal losses of the resonator, the lower the losses the higher the effective resistance. Hence in the case of an ideal lossless superconductor  $R \rightarrow \infty$ .

In order to find the magnitude of the transmission when it is minimum (i.e. at resonance) we must first define the scattering parameters. When dealing with an N-port network designed to measure incident, reflected, or transmitted waves in a

microwave circuit it is useful to use the scattering matrix formalism to relate the voltage waves incident on the ports to the reflected waves from the ports [42]. In practice these scattering parameters are measured using a Vector Network Analyzer (VNA). A specific element of the scattering matrix is defined as:

$$S_{ij} = \left. \frac{V_i^-}{V_j^+} \right|_{V_k^+ = 0, k \neq j} \quad (3.36)$$

where  $V_i^+$  is the amplitude of the incident voltage wave on port  $i$  and  $V_j^-$  is the amplitude of the voltage reflected wave coming out of port  $j$ . A key condition is that the incident waves on all ports except the port  $j$  are zero. Now that we have introduced the scattering parameters we can consider our particular case of a parallel RLC resonator measured by a two-port network as illustrated in Figure 3.7 c),d). At the resonance frequency of the resonator we obtain:

$$\frac{V_{out}}{V_{in}} = \frac{Z_{RLC}(\omega_0)}{2Z_{RLC}(\omega_0) + Z_0} \quad (3.37)$$

Then, normalizing to full transmission off resonance (i.e.  $S_{21}(\omega \ll \omega_0) = S_{21}(\omega \gg \omega_0) = 1$ ), and taking into account that the impedance of the RLC resonator at resonance is  $Z_{RLC}(\omega_0) = R$ , the transmission reads:

$$S_{21}(\omega_0) = \frac{2V_{out}}{V_{in}} = \frac{2R}{2R + Z_0} \quad (3.38)$$

It is common to express the magnitude of the transmission in dB as  $20 \log_{10} |S_{21}|$ . Thus, it is straightforward to show using Eqn. 3.38 that for the ideal lossless limit  $R \rightarrow \infty$  the transmitted power is 0 dB at resonance. When the resonator is capacitively coupled to the feedline we must take into account the effect of the coupling capacitance as detailed in Section 3.2.3, in which the impedance of the  $C_c$ -RLC system becomes  $Z_T = Z_{C_c} + Z_{RLC}$ . In that scenario we obtain:

$$S_{21}(\omega_0) = \frac{2Z_T(\omega_0)}{2Z_T(\omega_0) + Z_0} \quad (3.39)$$

An alternative way of expressing Eqn. 3.39 is [44] [45]:

$$S_{21}(\omega_0) = \frac{Q_c}{Q_c + Q_i} \quad (3.40)$$

This quantity represents the minimum transmission of a parallel RLC resonator in a two-port network, and it is essential to estimate an upper limit for the number of photons in the resonator, as will be further detailed in Section 3.2.5.

### 3.2.5 Number of photons in the resonator

In order to estimate the photon number in our resonators, we use the transmission of the parallel RLC system at resonance derived the previous section:

$$S_{21}(\omega_0) = \frac{Q_c}{Q_c + Q_i} \quad (3.41)$$

From Equation 3.41 we can extract an additional scattering parameter [42]:

$$S_{11}(\omega_0) = S_{21}(\omega_0) - 1 = \frac{-Q_i}{Q_c + Q_i} \quad (3.42)$$

Then, the reflected and transmitted powers are given by [9]:

$$P_{refl} = P_{in}|S_{11}|^2 \quad (3.43)$$

$$P_{trans} = P_{in}|S_{21}|^2 \quad (3.44)$$

where  $P_{in}$  is the input power and we do not account for impedance mismatches in the measurement setup. The power absorbed by the resonator reads:

$$P_{abs} = P_{in} - P_{refl} - P_{trans} = \frac{2Q_T^2}{Q_c Q_i} P_{in} \quad (3.45)$$

On the other hand, the power absorbed by the resonator can be expressed as a function of the average photon number, the microwave photon energy, and the energy loss rate [9]:

$$P_{abs} = \langle n_{ph} \rangle \hbar \omega_0 \frac{\omega_0}{Q_i} \quad (3.46)$$

Finally we can combine equations 3.45 and 3.46 to obtain an upper limit (due to unavoidable reflections in the input line) of the number of photons of the resonator as a function of the input power:

$$\langle n_{ph} \rangle = \frac{2}{\hbar \omega_0^2} \frac{Q_T^2}{Q_c} P_{in} \quad (3.47)$$

# Chapter 4

## Design and Fabrication

In this chapter we introduce the main features of the design of our lumped-element superconducting resonators. First we will describe each component of the design and define the main geometric parameters that affect the resonator's performance. Afterwards, we will focus on how the microwave circuit properties of the resonator can be simulated using finite element method software. We then show the different chip designs, every one of them focusing on studying a separate geometric parameter of the resonator. Finally we review the fabrication process of every device.

### 4.1 General design of a superconducting lumped element resonator

The geometry of our lumped element resonator is shown in Figure 4.1 a). As detailed in Section 3.1.2, an inductor can be reproduced by a short-circuited transmission line. In our design the inductor transmission line is formed by a meandered microstrip shaded in green (false color) in the figure. The main parameters determining the geometry of the inductor are shown in Figure 4.1 b) and d). In order to minimize the area of the inductor the distance between meander turns ( $d$ ) and the length ( $h$ ) of such turn have to be carefully selected. In our design we chose  $d = 2 \mu\text{m}$  so that the turns were as close as possible without too much reduction of the total inductance due to negative mutual inductance [46]. Moreover the edge of the turn, defined by  $h$ , needs to limit the gap between the meander and the ground plane, so that no parasitic capacitance arises. In the last place we have the width of the meander and the number of meander turns, both parameters will be selected depending on the geometric parameter that wants to be studied.

The capacitance in our LE resonator is comprised by the capacitor's pad shaded

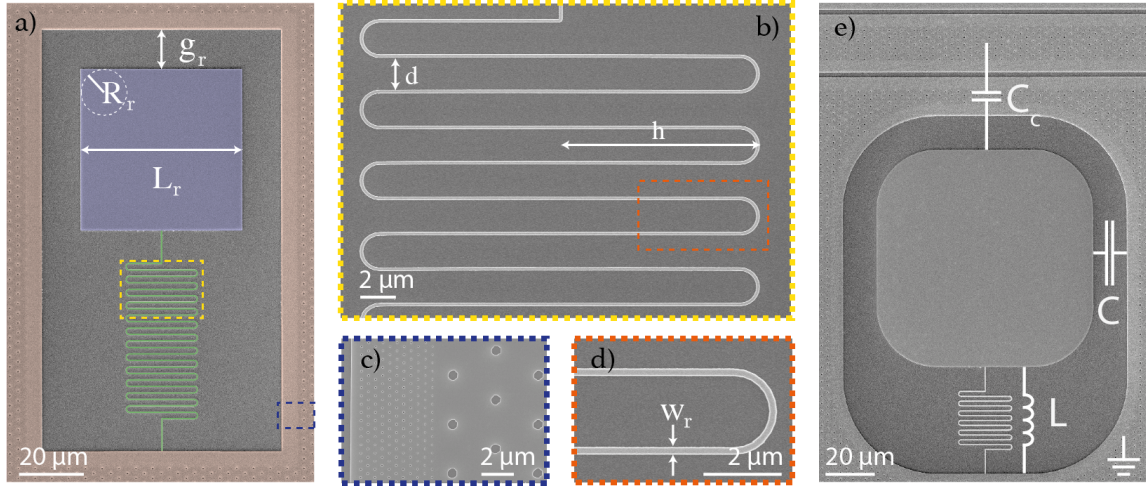


Figure 4.1: SEM images. Gray region corresponds to NbTiN while dark region corresponds to the HiRes Silicon substrate: a) Main design of the lumped element resonator in false color. The capacitor's pad is shaded in blue, the inductor is shaded in green, and the ground is shaded in red. b) and d) show a close up of the meander inductor, indicating its design parameters. c) Patterned holes on the ground plane for vortex pinning. e) Lumped element resonator capacitively coupled to the feedline showing the equivalent circuit model.

in blue (false color) and the surrounding ground planes shaded in red (false color) in Figure 4.1 a). This geometry models the open-circuited transmission line described in 3.1.2. The capacitance of this system is determined by the pad size ( $L_r$ ), the radius of the pad's edges ( $R_r$ ), and more importantly by the gap between the pad and the ground plane ( $g_r$ ). At last, an additional parameter governing the coupling quality factor is the spacing between the resonator and the feedline.

All the parameters mentioned above play a role in the resonance frequency of the resonator and in its coupling quality factor, as will be further detailed in Section 4.2. In Figure 4.1 e) is illustrated how every component form together a parallel LC resonator coupled through a capacitance  $C_c$  to the feedline.

### 4.1.1 Artificial pinning sites

The design is patterned on a NbTiN (Niobium Titanium Nitride) thin film of 20 nm thickness. Such material corresponds to the family of type II superconductors and has been frequently used for high quality resonators [9] [10] since it exhibits very low dissipation. Nevertheless, superconductors (in particular type II) rarely expel

completely an applied magnetic field out of its bulk. This is usually caused by grain boundaries or other types of defects, which trap the magnetic flux within the superconductor [47][48]. The trapped flux arises in the form of quantized tubes of flux, the so-called *Abrikosov vortices*. These vortices when trapped in the vicinity of the resonators provide another loss channel, and thus reduce the resonator quality factor [33]. Different efforts have been focused on minimizing this loss channel by trapping and pinning the flux lines either in a slot in the center of a CPW resonator [49] or in artificial defects (antidots) at the resonator edges [50]. Consequently our design incorporates artificial pinning sites in the form of antidots arranged in an hexagonal lattice (c.f. Fig. 4.1 c)), since that is the minimal energy configuration for such array of vortices [13]. Nonetheless, these artificial defects only trap vortices up to a finite applied field [10] and a critical current [13].

## 4.2 Simulation approach

In order to simulate the resonance frequency and the coupling quality factor of a particular resonator it was used the Microwave Office software [51], which uses a finite element method to solve Maxwell equations of a particular structure from its physical geometry. For the resonator design it is essential to know the inductance of the inductor, which is mainly kinetic and described by Eqn. 2.25. In order to get an estimate of the kinetic inductance of the film, we extract the sheet resistance of the film via the 4-probe method at room temperature and we take the approximate critical temperature of the thin film to be  $T_c \approx 10\text{ K}$  [52]. Then using Eqn. 2.25 we obtain  $L_k \approx 14.8\text{ pH}/\square$ .

The transmission line responsible of propagating TEM waves across the chip has the configuration of a coplanar waveguide (c.f. Fig. 2.1). In order to reduce asymmetries in the resonance peaks of the resonators, the dimensions of the feedline have to be properly selected according to impedance matching. In other words, the impedance of the feedline must be  $50\Omega$ . Taking the characteristic impedance of the transmission line as  $Z_0 = \sqrt{L/C}$  (see Section 3.1.1), and the inductance and capacitance of the CPW from Eqn. 2.26, 2.27 and Eqn. 2.28 respectively, we find impedance matching dimensions for  $L_k \approx 14.8\text{ pH}/\square$  to be  $s = 2\mu\text{m}$  and  $W = 29.4\mu\text{m}$ . Note that this dimensions will be re-adapted from chip to chip according to the measured  $L_k$ .

The simulation process consists in simulating the transmission through the feedline and extracting the resonator's response ( $f_r, Q_c, Q_i$ ) from the resonances with the diameter correction method [45]. Such fitting method is also used to fit the measured transmission data, since it tolerates a high asymmetry in the resonance peak. The

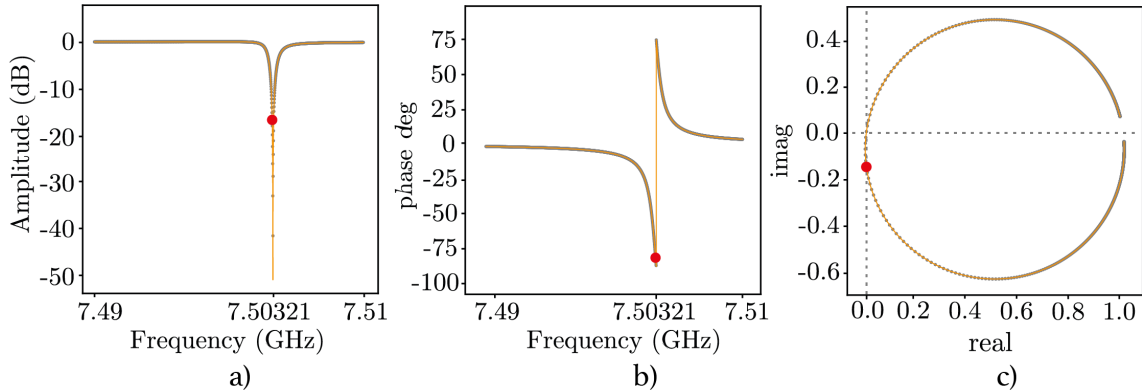


Figure 4.2: Response of the resonator depicted in Fig. 4.3, data points are shown in grey, fit is shown in orange and red dot shows the resonance frequency.: a) Transmission amplitude in dB. b) Transmission phase in degrees. c) Imaginary and Real part of the transmission.

general form of the transmission resonance accounting with a number of non-ideal factors is [45]:

$$S_{21} = A \left( 1 - \frac{\frac{Q_T}{|Q_e|} e^{i\theta}}{1 + 2iQ_T \frac{f-f_r}{f_r}} \right) \quad (4.1)$$

with  $f_r$  the resonance frequency,  $A$  the transmission amplitude not in resonance,  $Q_T$  the total quality factor of the resonator (see Eqn. 3.34), and  $Q_e = |Q_e|e^{-i\theta}$  is a complex quantity defined as  $1/Q_c = \Re\{1/Q_e\}$ . The asymmetry of the resonance stems from the complex loading of the resonator, and it is quantified here by  $\Im\{1/Q_e\}$ . The typical measured/simulated response of a parallel RLC resonator around its resonance frequency is shown in Figure 4.2. The orange continuous line shows the result of the fit from which we extract the resonator properties.

When designing a chip with multiple resonators coupled to the same feedline, it is desired that the resonance frequencies of all resonators are evenly spaced out in frequency such that we can later identify which resonator corresponds to what resonance and such that the resonance can be accurately fitted. Moreover the quality factor of all resonators is chosen to be  $Q_c \sim 10^4$ , so that we can compare among resonators in a consistent way.

It is important to corroborate that in fact our design can be treated as a lumped element resonator. With this aim we perform current density simulations in our resonator at two different frequencies. Off-resonance, shown in Figures 4.3 a),c), the current density is highest at the feedline, while on-resonance, shown in Figures 4.3

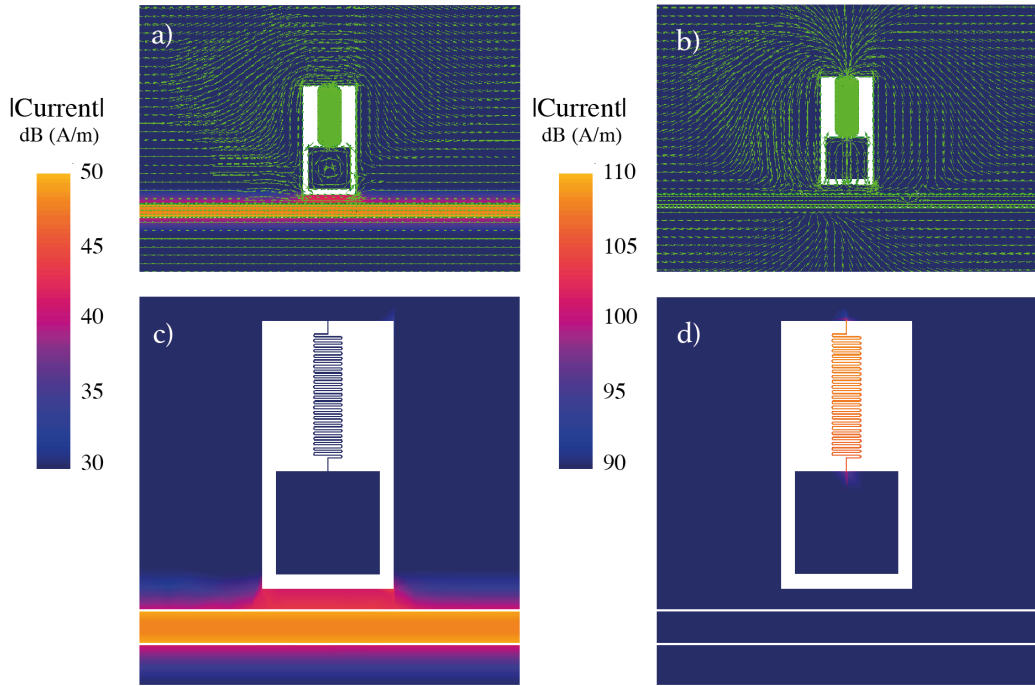


Figure 4.3: Current density distribution obtained with Microwave Office at two different frequencies. a) and c) Current density distribution at  $f = 2\text{ GHz}$  Most current is localized at the waveguide. b) and d) Current density distribution at the resonance frequency of the resonator  $f = f_r = 7.5\text{ GHz}$ , most current is now localized at the meander inductor. The green arrows in a),b) show the current direction.

b),d), the current is mostly located at the meander inductor, validating this way the lumped element model.

A complementary approach which gives further insight on the resonator's response consists in using COMSOL [53] to simulate capacitances  $C$  and  $C_c$ . From these simulated values we can calculate the coupling quality factor using equation 3.35 from Section 3.2.3. Secondly we can calculate the total inductance of the resonator by using the estimated kinetic inductance per square and the total number of squares in the inductor (length/width). Knowing the inductance and capacitances of the resonator we can obtain its resonance frequency. This approach leads to a lower accuracy in the value of resonance frequency, since it does not take into account any current dynamics, however it serves as a tool faster than Microwave Office to obtain rough estimates.

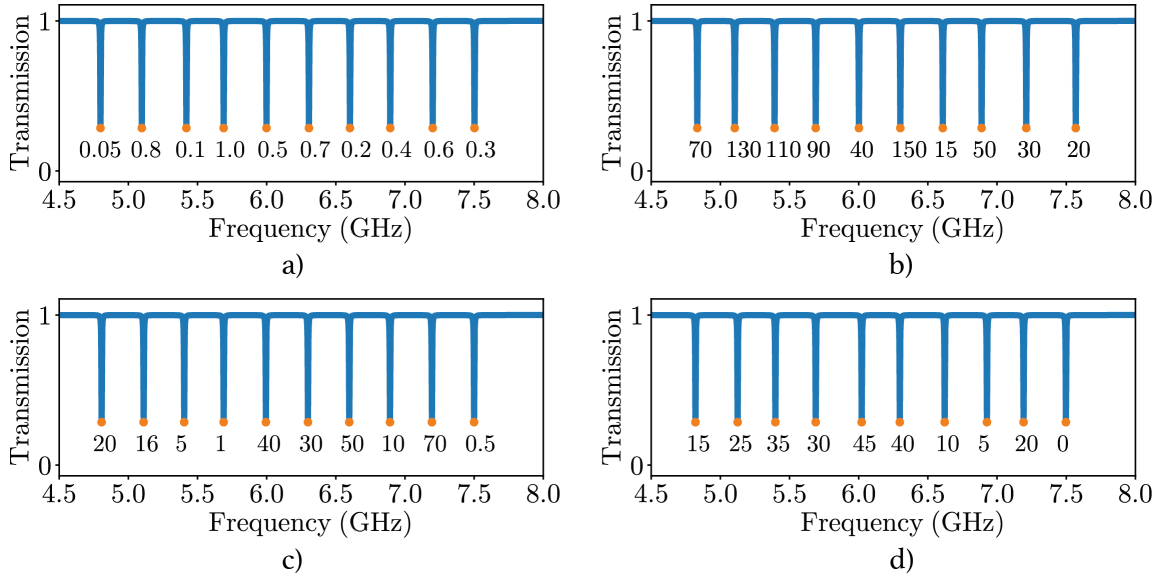


Figure 4.4: Designed transmission for every chip. a) Chip with varying inductor's width. Each resonance has indicated below its resonator's inductor width ( $\mu\text{m}$ ). b) Chip with varying capacitor's size. Each resonance has indicated below its resonator's capacitor's size ( $\mu\text{m}$ ). c) Chip with varying resonator's gap. Each resonance has indicated below its resonator's gap ( $\mu\text{m}$ ). d) Chip with varying capacitor's pad edge radius. Each resonance has indicated below its resonator's capacitor edge radius ( $\mu\text{m}$ ).

### 4.3 Chip designs

In this section we present the design of four chips. Each chip aims to study a different geometric parameter: the inductor's width ( $W_r$ ), the capacitor's pad size ( $L_r$ ), the resonator's gap ( $g_r$ ) and finally the capacitor's pad edge radius ( $R_r$ ). In order to make sure any potential trend in  $Q_i$  versus geometric parameter really stems from the geometry of the resonator, it was imposed in the design the uncorrelatedness between parameter under study and resonance frequency (c.f. Figure 4.4), as well as parameter under study and position of the resonator in the chip. Moreover, in order to design many resonators with a wide range of different geometries we study the effect of the main geometric parameters on the resonator's response ( $f_r, Q_c$ ).

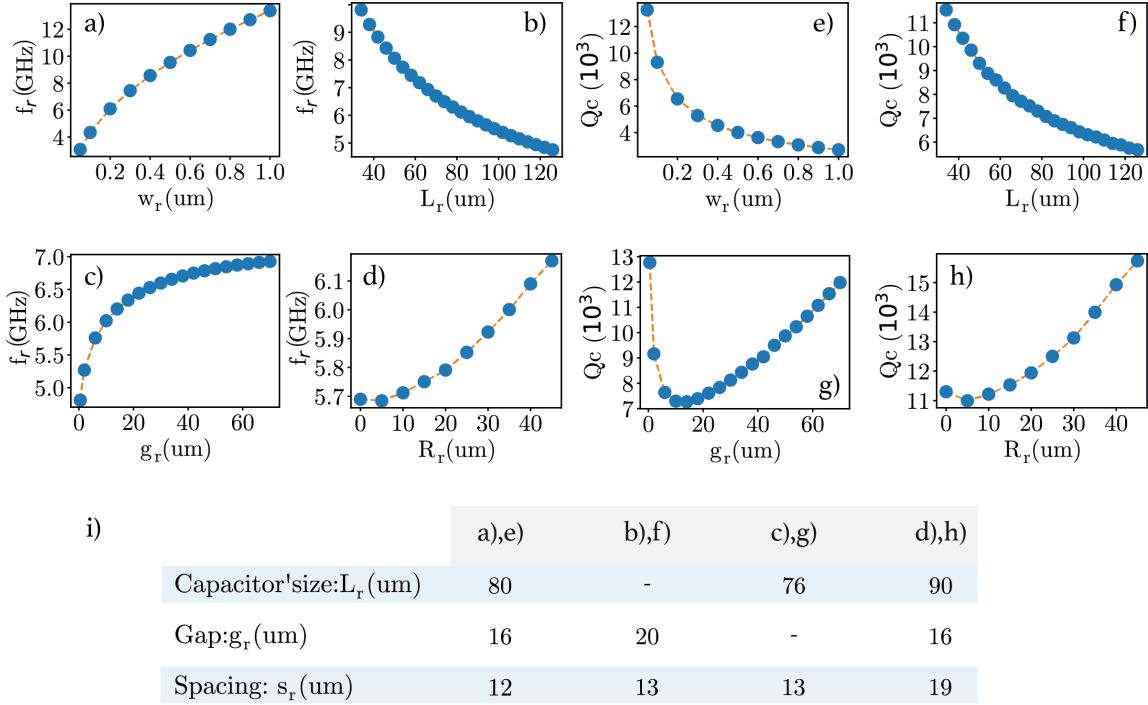


Figure 4.5: Simulated  $f_r$  and  $Q_c$  with Microwave office at  $L_k = 11.0 \text{ pH}/\square$ . The orange line is a guide for the eye. Resonance frequency (Coupling quality factor) depending on the a) (e)) inductor's width, b) (f)) capacitor's size, c) (g))resonator's gap, d) (h))capacitor's edge radius. i) Table indicating the resonator's features used for every parameter simulation. Spacing refers to the distance between the resonator and the feedline. All resonators have 8 meander turns and an inductor's width of  $W_r = 0.2 \mu\text{m}$  (unless  $W_r$  is the varying simulation parameter). Likewise all capacitor pads are squared ( $R_r = 0 \mu\text{m}$ ) unless the edge radius  $R_r$  being the varying parameter.

### 4.3.1 Design 1: 10 resonator inductor's width dependence

The first design intends to make the inductor's width the main geometric feature differentiating all resonators, as illustrated in Figure 4.6 a). The width of the inductors ranges from  $0.05 \mu\text{m}$  to  $1 \mu\text{m}$ , which comprise more than one order of magnitude (see Figures B.2 d),e),f) in Appendix B). As previously mentioned, the total kinetic inductance depends on the total number of squares in the inductor, being one square the ratio of the length and width of the inductor. Therefore, when increasing the width of the inductor while keeping the rest the same, the total number of squares decreases, and with it the the total inductance. This increases the resonance frequency of the resonator, as illustrated in Figure 4.5 a). For that reason the length of

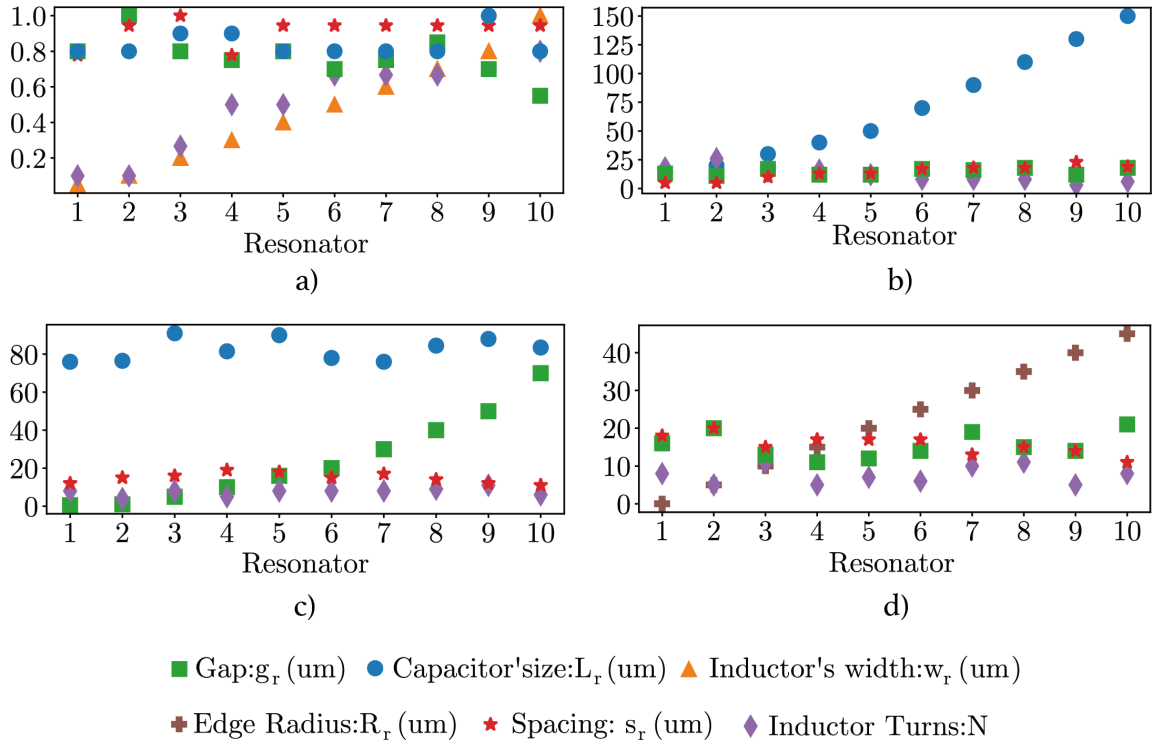


Figure 4.6: Main design parameters for every resonator in the four designed chips. A parameter missing in the figure means it is constant throughout all resonators. a) Chip with varying inductor's width, the values are normalized to illustrate how the main parameter (inductor's width) is the one varying the most. b) Chip with varying capacitor's size. c) Chip with varying resonator's gap. d) Chip with varying capacitor's pad edge radius.

the inductor (or the number of meander turns) has to increase to keep the resonance in the desired frequency range.

### 4.3.2 Design 2: 10 resonator capacitor's size dependence

The second design focuses on the capacitor's size, the smallest being  $15 \mu\text{m}$  and the largest  $150 \mu\text{m}$ . Figure 4.6 b) shows how the capacitor size is the most distinctive parameter of every resonator. This characteristic can be seen in the actual resonator's design, as illustrated in Figures B.2 a),b),c) in Appendix B. Figures 4.5 b),f) depict the effect of the capacitor's size in the resonator response. For larger capacitor pads we find lower resonance frequencies and lower coupling quality factors, due to the capacitance increasing with capacitor's size.

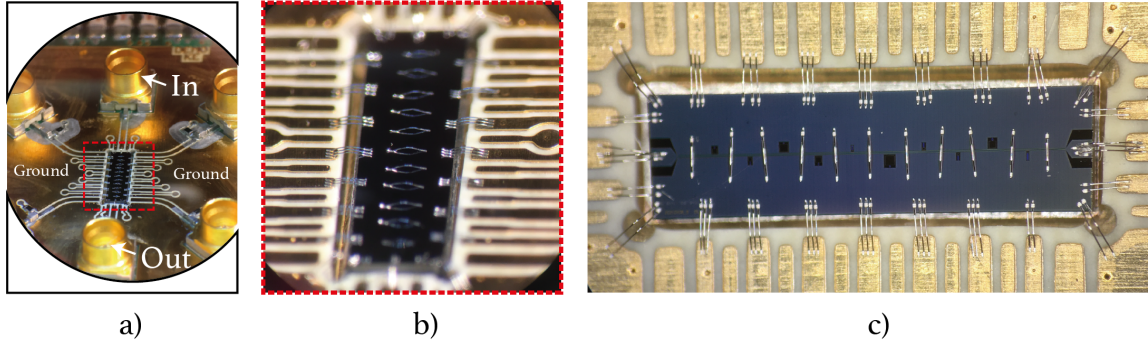


Figure 4.7: a) Chip bonded to the PCB. Labels indicate the input, output pins and the ground plane of the PCB. b) Zoom in of the bonded chip. c) Top view of the bonded PCB, showing the aluminium wires bonding the chip’s ground planes to the PCB ground planes, bonding the chip’s launchers to the input and output lines of the PCB, and finally interconnecting both ground planes of the chip. Resonators can be seen as square black spots due to the etched out NbTiN.

### 4.3.3 Design 3: 10 resonator gap dependence

In third place we focus on the gap between the capacitor’s pad and the ground planes, denoted by  $g_r$ . There are two orders of magnitude between the smallest ( $0.5 \mu\text{m}$ ) and the biggest ( $70 \mu\text{m}$ ). The gap increases while keeping the other parameters as constant as possible (see figure 4.6 c)). By increasing the gap we decrease the capacitance of the resonator, this is reflected in the resonance frequency dependence on  $g_r$  in Figure 4.5 c). The capacitance approaches zero as the gap is increased to infinity, which is why we can see how the resonance frequency saturates for large gaps.

### 4.3.4 Design 4: 10 resonator capacitor’s edge dependence

Finally the fourth design revolves around how round is the edge of the resonator’s capacitor (see Fig. 4.6 d)). The smallest edge radius ( $0 \mu\text{m}$ ) corresponds to a square pad while the biggest edge radius ( $45 \mu\text{m}$ ) corresponds to a circular pad (c.f. Fig. B.2 g),h),i) in Appendix Bd)). The size of the pad is kept constant for all resonators at  $90 \mu\text{m}$ . The capacitor’s shape transformation leads to a parabolic increase of resonant frequency and coupling quality factor shown in Figures 4.5 d),h).

## 4.4 Device Fabrication

The design is patterned on a 20 nm thick NbTiN (Niobium Titanium Nitride) film lying on a HiRes Silicon wafer. The NbTiN thin film is deposited on the wafer using the sputtering technique. After applying the proper resist, the pattern is written using a single electron beam lithography step. Following the development of the pattern, RIE etching is used to carve the design on the NbTiN film. Finally the chip is diced and cleaned and ready to bond to the Printed Circuit Board (PCB) with aluminum wire bonds. The full fabrication recipe can be found in Appendix B.

# Chapter 5

## Measurement Setup

In order to characterize superconducting resonators with minimum thermally induced quasiparticle loss [54], it is necessary to make the measurements at temperatures lower than one-tenth of the critical temperature ( $T_c$ ) of the electrode material [6]. For that reason the resonators are placed in a dilution refrigerator, whose standard base temperature is around 20 mK for an indefinite period of time. Moreover, with the aim of reducing noise and to increase thermal isolation many signal attenuators are used. Consequently, amplifiers are placed in the output line to make possible VNA measurements. In this section we briefly describe the circuitry used to achieve the desired cryo-measurements.

### 5.1 Measurement procedure

A dilution refrigerator is a device capable of creating an environment with extremely low temperatures (few mK). This is an essential condition for our resonator measurements, since we need our material in its superconducting state and with minimum thermally induced losses. Figure 5.2 shows the dilution refrigerator wiring diagram used in this work. Particularly intended for resonator readout at millikelvin temperatures. The device responsible of signal excitation and readout is the so-called Vector Network Analyzer (VNA). The signal that comes out of its input port (P1) needs to be heavily diminished, hence many attenuators are placed in different temperature stages. In order to reach the single photon power level there is a 95dB added attenuation in the input line [55]. In addition, every attenuator aims to reduce noise at every stage. On the other hand, the output signal needs to be sufficiently amplified for VNA measurements. This is achieved with the help of a High Electron Mobility Transistor (HEMT) at 5 K and a room temperature amplifier. However, the HEMT may be an additional noise origin, therefore a circulator is placed to protect the res-

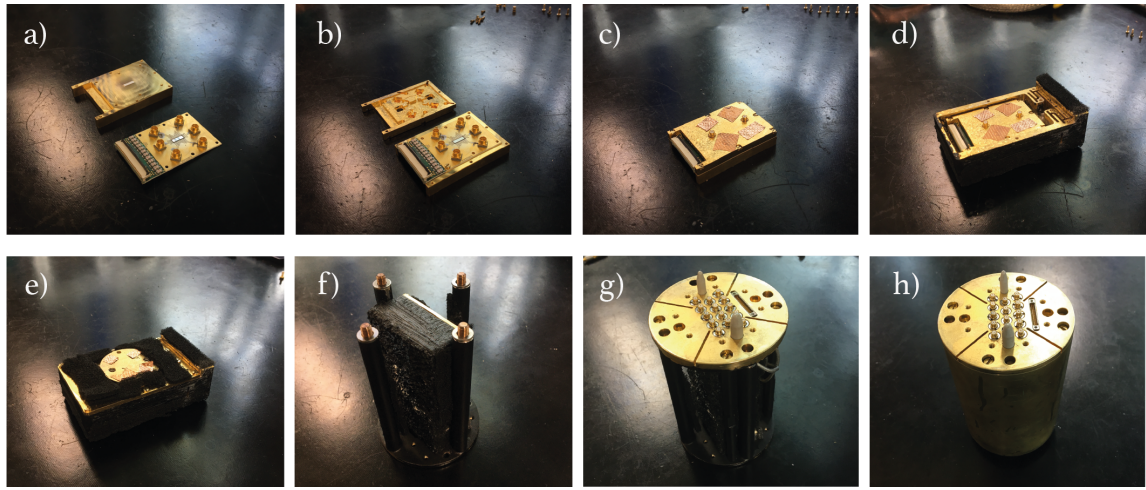


Figure 5.1: Multi packaging of the device: a) Top: Bottom metallic block onto which the chip is glued with silver paint, thus helping the thermalization of the chip. Bottom: Chip bonded to the PCB. b) Top: Lid of the inner enclosure box. Bottom: PCB attached to the bottom block using various screws. c) Inner PCB enclosure/shielding box. d) Inner PCB enclosure/shielding box placed inside an outer enclosure box. Foams and black paint shield from external radiation. e) Outer PCB enclosure/shielding box. f) Outer enclosure box placed in puck's base. g) Input and output lines of the puck are connected to the input and output pins of the shielding box using RF coaxial cables. h) Puck with its radiation shield.

onators from such noise. Note that there is a TWPA amplifier located in the output line as well. The TWPA requires an additional pump tone depicted in the schematic, however for our measurements there is no need for such amplifier and the pump is off.

In order to connect the room temperature part of the refrigerator to the 5 K plate, stainless steel coaxial cables are used, its advantages being low loss and adequate thermal conductivity. For the next temperature stages, the cables are made of NbTi, so as to further reduce loss and improve thermal isolation. Finally, copper cables are used to connect the base plate to the puck.

The sample is bonded to a Printed Circuit Board (PCB), which is later placed in multiple packaging (c.f. Figure 5.1) that provide thermal shielding and IR absorption to avoid losses due to RF induced quasiparticles [6]. SMP female-female adapters (bullets) [56] are placed on the input and output ports of the PCB to connect them to the outer enclosure stages. Next we further detail the purpose of each shielding

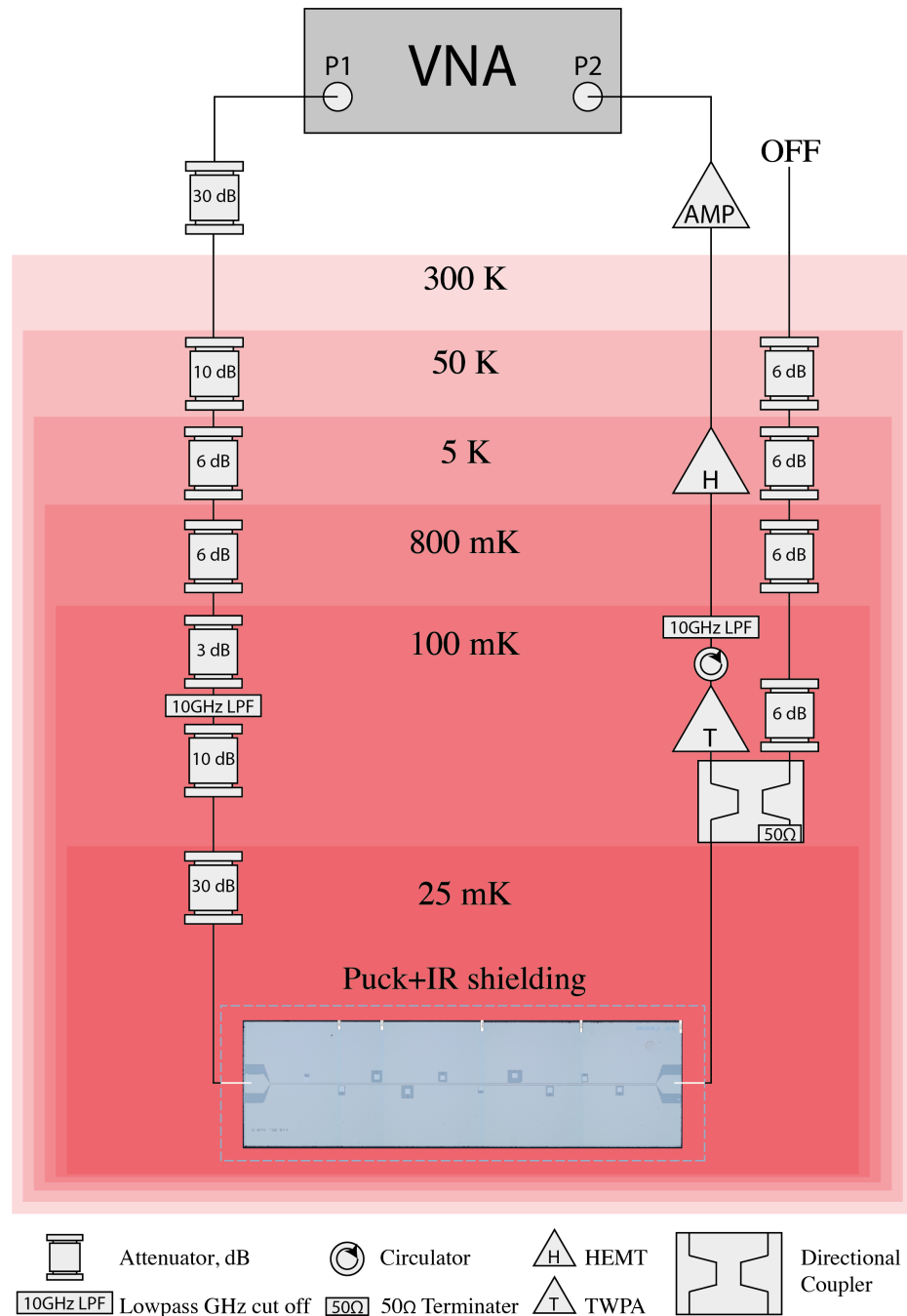


Figure 5.2: Schematic of the measurement setup.

component.

The inner enclosure box, depicted in Figure 5.1 c), aims to shield stray radiation. This small box is inserted into a bigger (outer) enclosure box, as illustrated in Figure 5.1 d). The outer box is covered with a special black paint [57] and a purpose-built foam [58]. The foam is a microwave absorber which ensures absorption in the 5 GHz-90 GHz range [58]. It dampens any mode that might exist in the boxes (due to cavity-like behaviour caused by reflective surfaces), and slightly absorbs infrared. The infrared radiation we want to greatly avoid is typically towards higher frequencies, where the foam does not perform as well. Moreover the foam does not thermalize effectively, and its absorbed energy is not properly dissipated. For that reason a special black paint covering the enclosure box is used. Such black paint is a mixture of carbon black and stycast, which are materials that absorb the relevant infrared frequencies and are good thermal conductors [57]. In addition, the mixture contains silicon carbite (SiC) grains of 1 mm, intended to make the surface more coarse so that the light does not bounce off in a 90° angle, but it diffuses across the absorber and stays there for a relatively long period of time, increasing this way the absorption rate. In practice, longer stray light wavelengths are harder to absorb [59], which is why thick absorbing layers are required. Here multiple layers of paint were applied. Finally Figure 5.1 h) shows an additional shield protecting the puck from radiation. In particular thermal radiation caused by the magnets used to produce magnetic fields, since these magnets are at a relatively high temperature ( $T_{magnet} \approx 4.9\text{ K}$ ) and there is no low-temperature shield separating them from the puck.

## 5.2 Field alignment

To apply in plane and out plane magnetic fields, we use three coil magnets that apply magnetic field in the  $x, y, z$  components respectively, see Figure 5.3 b). Tuning the three components of the magnetic field we can obtain any resulting magnetic field's magnitude and direction with respect to the sample. Nonetheless, the sample inside the dilution refrigerator has a certain orientation with respect to the magnets axis. Hence, it is necessary to properly align the field with the sample before doing any experiments. The perpendicular field needs to be monitored at all times during the aligning process, making sure it stays as low as possible to not introduce vortex related losses. Therefore, the first step consists in just applying a magnetic field in the  $z$  component of the magnet (Fig. 5.3 c)), which should have a small out of plane component. Note that we use spherical coordinates for the field alignment. Secondly we apply a small angle  $\theta$  to slightly increase the out of plane component (Fig. 5.3 d)). At that same angle  $\theta$  we measure the resonance frequency of all resonators versus angle  $\phi$ . Due to the influence of the magnetic field over the kinetic inductance, the resonance frequency will follow a sinusoidal shape with  $\phi$  (see Fig. C.1 a) in Appendix C). At the sweet spot ( $\phi^*$ ) where the resonance frequency is lowest the out of field component will be maximum (Fig. 5.3 e)). At such angle we will sweep angle  $\theta$ , and monitor the resonance frequency of all resonators to find the angle  $\theta_{in}$  where  $f_r$  is highest (see Fig. C.1 b) in Appendix C), and thus the in plane field component is maximum (Fig. 5.3 f)). Hence, the angles  $(\theta, \phi) = (\theta_{in}, \phi^*)$  correspond to the in plane field component (Fig. 5.3 g)), while the angles  $(\theta, \phi) = (\theta_{in} + 90^\circ, \phi^*)$  (Fig. 5.3 h)) correspond to the out of plane field component.

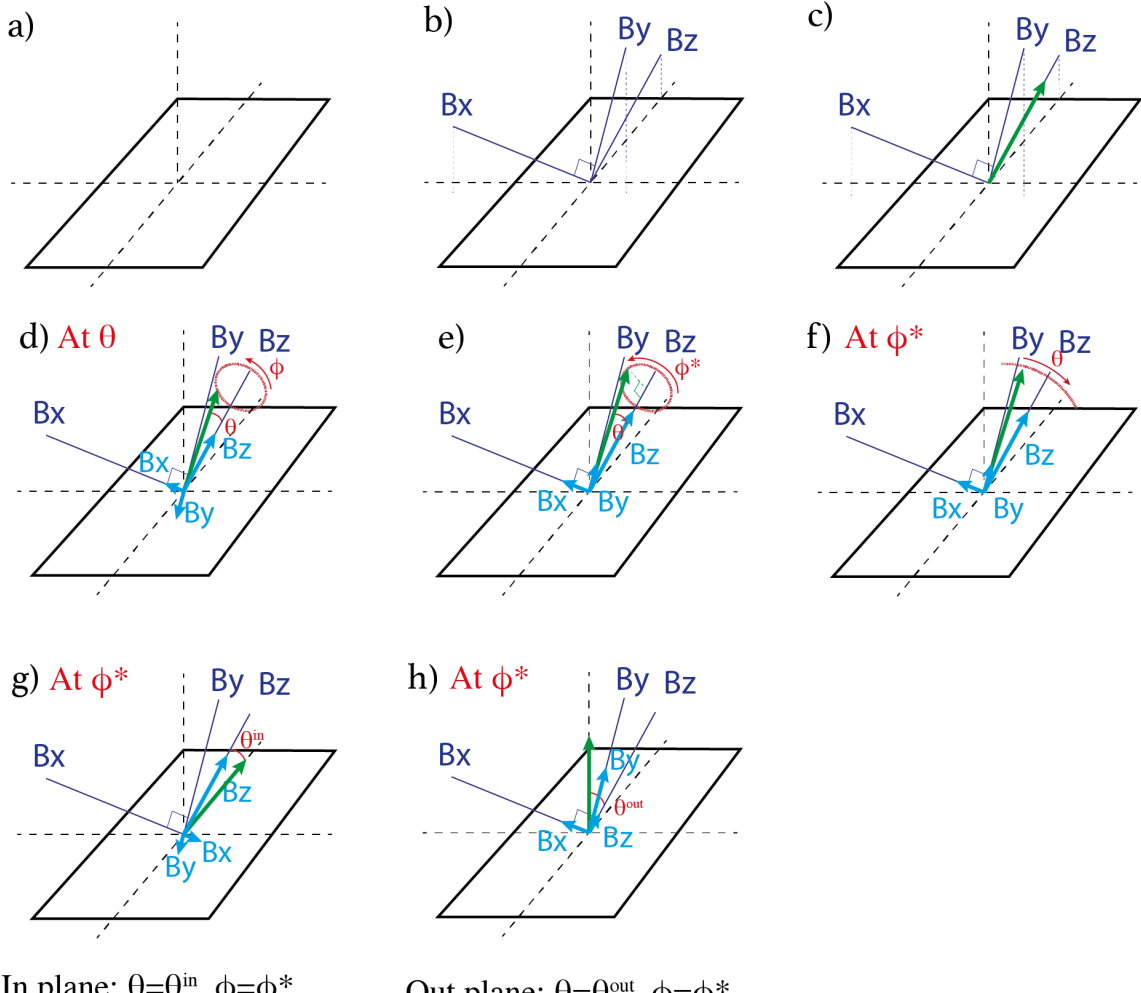


Figure 5.3: Alignment of the magnetic field with the sample: a) Sample and its axis. b) Magnetic fields axis. c) First apply magnetic field solely on the z direction. d) In spherical coordinates, rotate the magnetic field a small angle  $\theta$ . e) Sweep angle  $\phi$  and find the  $\phi^*$  that minimizes the resonant frequency, thus maximizes out of field component. f) At angle  $\phi$  sweep angle  $\theta$  to find  $\theta$  that maximizes in plane field component. g) B field components that result in the in plane magnetic field with respect to the sample. h) B field components that result in the out of plane magnetic field with respect to the sample.

# Chapter 6

## Measurement Results

Despite resonators being superconducting and therefore having low losses, there are still some loss channels diminishing the intrinsic performance of superconducting resonators. In practice, the most significant loss forms in superconducting microwave resonators are two-level systems (TLS), magnetic field induced vortices, radiation and quasiparticles stemming from light and microwave induced pair-breaking [6]. Loss mechanisms for superconducting resonators is a relevant field of study, since their performance are crucial in qubit applications as well as in kinetic inductance detectors for astronomy applications. We start this chapter by associating the measured resonances with the corresponding resonator geometry through a transmission sweep at zero field. Next we show the extracted quality factors corresponding to every resonator design. Finally we present power and magnetic field dependent measurements to allow a full study on the role of resonator geometry in resonator losses.

### 6.1 Zero field transmission measurements

The first step in associating a resonator with its measured resonance is looking for the initially designed resonance frequency in the measured transmission spectrum. When it is unclear to what resonator does it correspond a particular resonance, it is necessary to re-simulate the resonator's response by adapting some design parameters to the observed ones. The parameters than vary the most from the initial design to the real device are the kinetic inductance and the inductor's width. The latter is obtained through a SEM inspection of the actual fabricated device, while the kinetic inductance can be manually tuned until simulations match measurements. Figure 6.1 b),a) show the initial transmission measurement and its corrected simulations counterpart for the chip in which we vary the capacitor's edge (see Appendix C for the other devices). Moreover in Figures 6.1 c),d),e) we display the measured

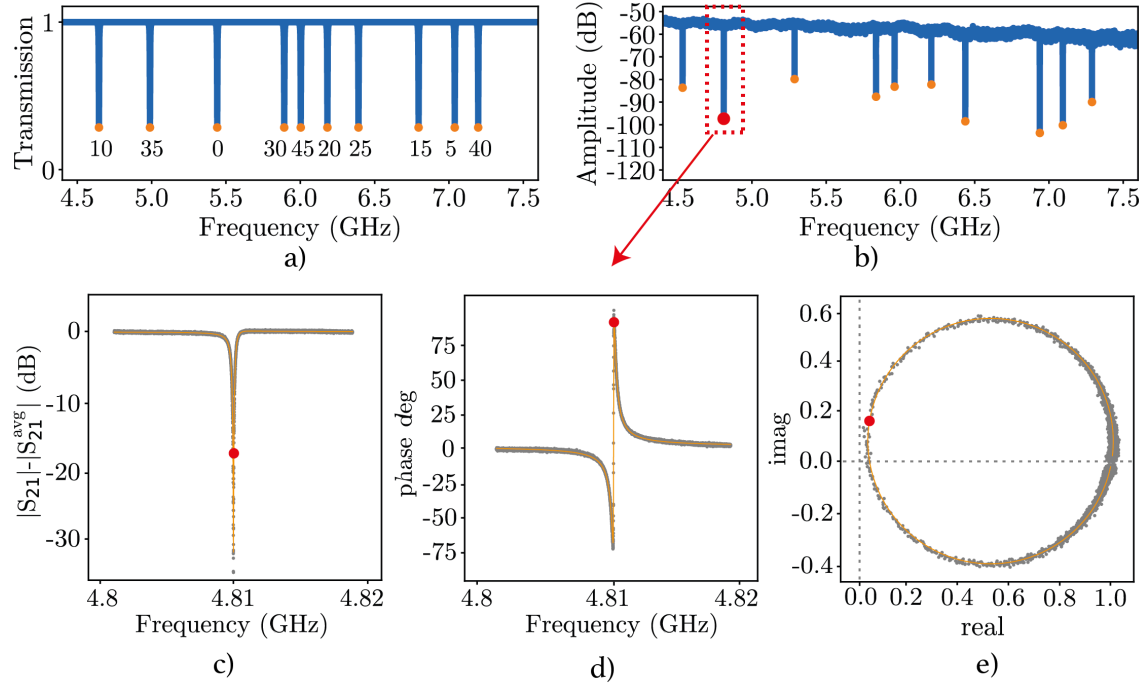


Figure 6.1: a) Simulated response of the 10 resonators with varying capacitor's edge radius after correcting the width of the inductor by SEM inspection of the actual measured device. b) Measured response of the 10 resonators with varying capacitor's edge radius. Response of the  $35\mu\text{m}$ -4.81 GHz resonator: c) Measured Transmission amplitude minus the transmission amplitude off-resonance in dB. d) Transmission phase in degrees. e) Imaginary and real part of the transmission. Data points are shown in grey while fit is represented by the orange line. Red dot shows the resonance frequency.

response of the resonator with  $35\mu\text{m}$  capacitor's edge radius. The gray markers denote the data points, while the fit is represented by the continuous orange line. With this representative case we highlight the resonator's response does not show strong impedance mismatch and therefore leads to reliable values of  $Q_c$ ,  $Q_i$  and  $f_r$ .

## 6.2 Geometry dependence at zero field

We extract the internal quality factor of each resonator  $Q_i$  by fitting the transmission spectrum around each resonance as detailed in Section 4.2. No conclusive correlation is observed between  $Q_i$  and capacitor's geometry within measurement variability (see

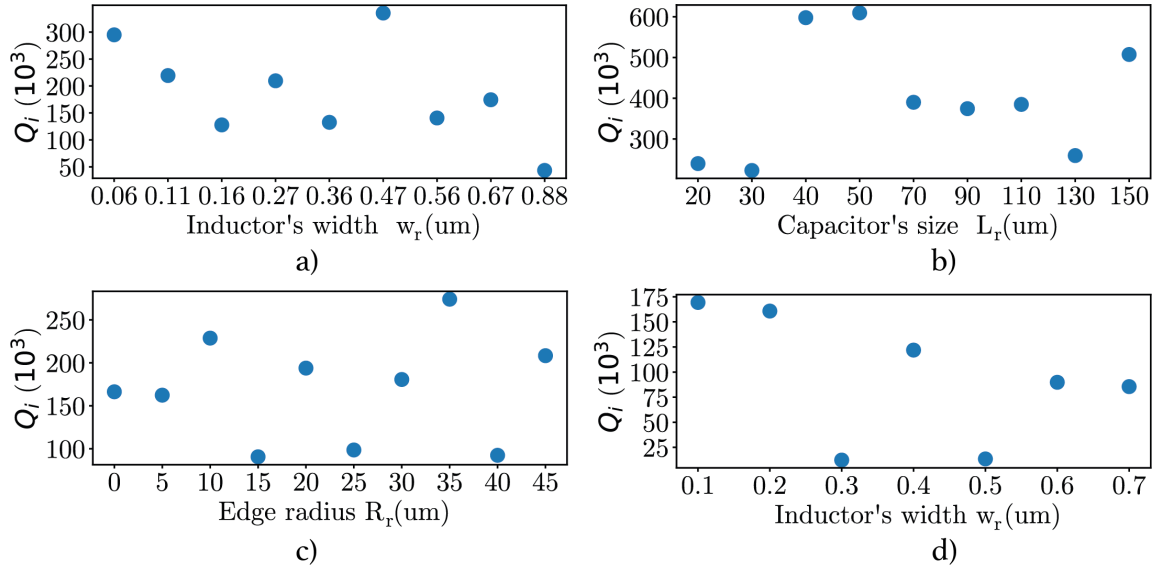


Figure 6.2: Measured  $Q_i$  for each chip at  $-10 \text{ dBm}$  at the power source output. The errorbars estimated from the fit are smaller than data points. a) Chip with varying inductor's width. b) Chip with varying capacitor's size. c) Chip with varying capacitor's edge radius. d) Chip with varying inductor's width.

Fig. 6.2 b) and c)). On the other hand, figures 6.2 a) and d) show that thinner inductors might lead to higher quality factors, however slight deviations from the trend entail further characterization of this effect is needed. We can also compare resonators at the same photon number (see Fig. C.5 in Appendix C). Nevertheless the ranking of  $Q_i$  remains similar throughout the entire photon number range.

The coupling quality factor remains similar for all resonators, as depicted in Figure C.3 in appendix C. We note that two fabricated chips with varying resonator's gap showed strong impedance mismatch resulting in inaccurate measurements, they are consequently not shown in this work.

### 6.3 Power dependence of SC resonators

The dependence of resonator loss on applied power is a fundamental way to study the origins of various loss mechanisms [6]. At  $T \ll T_c$  and single photon powers the dominant loss channel in resonators is known to be the two-level system coupling. The population of TLS saturate as power increases. Unfortunately most experiments in quantum computing are set close to the single photon limit, where the TLS

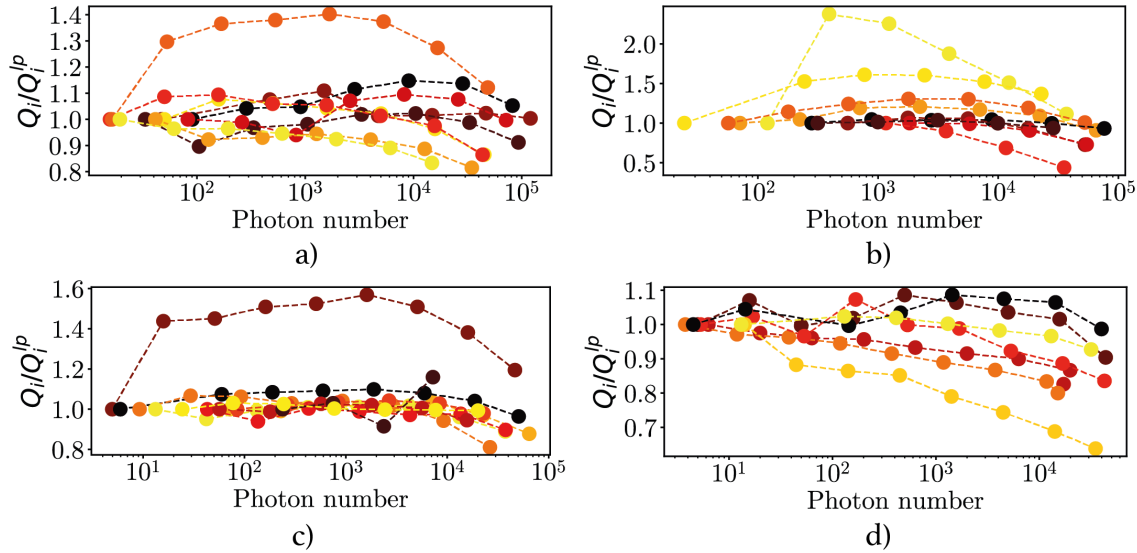


Figure 6.3: Intrinsic quality factor divided by the lowest photon number  $Q_i$ . a) Chip with varying inductor's width. Darker color marker corresponds to thinner inductor. b) Chip with varying capacitor's size. Darker marker color corresponds to smaller capacitor. c) Chip with varying capacitor's edge. Darker marker color corresponds to a more squared shape capacitor. d) Chip with varying inductor's width. Darker maker color corresponds to thinner inductor.

loss takes its maximum value. At higher powers however, where microwave kinetic inductance detectors operate [60], the microwave-induced quasiparticle loss governs the quality factor of the resonator.

The intrinsic quality factor shows a slight increase for some resonators at the very low power regime, see Figure 6.3. At medium power range the TLS are saturated and  $Q_i$  stays constant for a bit. Finally, at high powers we see a decrease in  $Q_i$  thought to be caused by the increase in quasiparticle loss. We observe that low-power-high- $Q_i$  resonators tend to increase at low powers, contrary to low-power-low- $Q_i$  resonators, which stay constant or decrease with increasing drive power (see Fig. C.5 in Appendix C).

Power loss at high powers is associated with the inductive part of the resonator, since it is where most current density is allocated. Figure 6.3 a) and d) show the performance of resonators with different inductor's width. Note that the thinner the inductor the darker the color of the marker. Figure d) shows that wide inductors are more susceptible to input power. Having established that the main loss form is quasiparticle loss, it could be that the wider the inductor the larger the population of

quasiparticles, and therefore the multiplication process described in Section 2.7.3 is more dominant. This trend might occur in Figure a) but with some slight deviations, thus further characterization of this phenomena is warranted.

Figure C.4 in Appendix C shows the estimated average photon number in dependence on the input power  $P_{in}$ . The logarithmic photon number scales linearly with the logarithmic input power with only one slope. This behaviour suggests the TLS systems are already saturated at low powers, and therefore the main loss source is microwave-induced pair-breaking. The red line in Figure C.4 accounts for the linear dependence of the photon number at both low and high power regimes:

$$\langle n_{ph} \rangle = 0.7 \cdot 10^{11} P_{in} [mW] \quad (6.1)$$

The observed overall behaviour can be understood by looking at Equation 3.47. Our resonators are in the regime  $Q_c < Q_i$ , allowing this way the approximation  $Q_T \approx Q_c$ . Since  $Q_c$  is power independent [38], then the average photon number will scale with drive power and increase with lower resonance frequency.

## 6.4 Magnetic Field

Superconducting microwave circuits for qubits and kinetic inductance detectors are frequently operated at relatively small fields. The performance of superconducting resonators under applied fields provide a simple way of studying magnetic field induced losses, and is therefore the motivation for the following sections. Here we will show parallel (in plane) and perpendicular (out of plane) magnetic field measurements and their analysis, aiming to shed light on the role of geometry on resonator resilience.

### 6.4.1 Parallel Magnetic Field

The performance of our lumped-element resonators to a parallel magnetic field is shown in Figure 6.4, which shows the dependence of intrinsic quality factor on  $B_{||}$ . The most visible feature is the dip in  $Q_i$  in the range 120 – 260 mT, consistent with previous results in NbTiN thin films [10]. Such dip is associated to a coupling of the resonator with an electron spin resonance (ESR), which increases losses in the cavity. The frequency of the dip scales with the resonance frequency of the resonator. In fact, using the condition for spin resonance  $\hbar\omega_0 = g\mu_B B_{min}$  [11] we can extract the Landé factor  $g \approx 2.14$ , as illustrated in Figure C.7 in Appendix C.

Our resonators appear to be resilient under parallel magnetic fields up to at least 1 T, magnitude that was limited by the maximum magnetic field allowed in

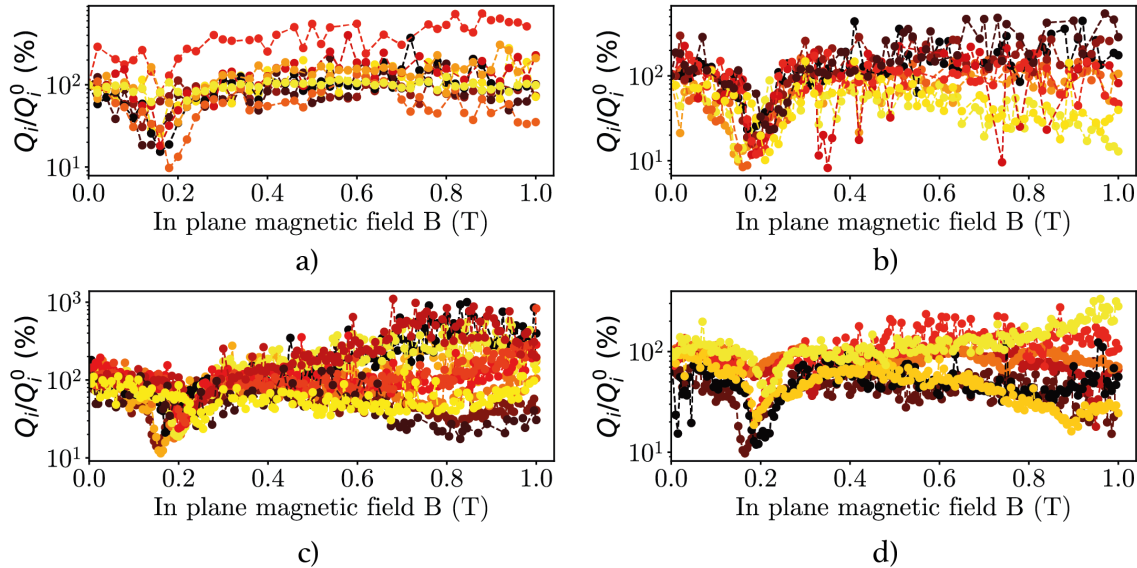


Figure 6.4: Intrinsic quality factor divided by the quality factor at zero field. a) Chip with varying inductor's width. Darker color marker corresponds to thinner inductor. b) Chip with varying capacitor's size. Darker marker color corresponds to smaller capacitor. c) Chip with varying capacitor's edge. Darker marker color corresponds to a more squared shape capacitor. d) Chip with varying inductor's width. Darker maker color corresponds to thinner inductor.

the measurement setup. Additional measurements (not shown due to misalignment of magnetic field and misfabrication subtleties) of our LC resonators in a different fridge suggested the  $Q_i \sim 10^5$  could be retained up to 5 T. Consistent with previous studies [10][11], we observe a slight enhancement in  $Q_i$  in the range 0.5 T-1 T. This has been attributed to the Abrikosov vortices in the superconducting film, which act as quasiparticle traps and thus reduce quasiparticle losses [10]. No clear trend for  $Q_i$  versus parallel field is observed in terms of capacitor's shape or inductor's width. Nonetheless Figure 6.4 b) seems to indicate that small capacitors (darker color markers) perform better at increasing in plane magnetic field. Since the main loss mechanism stems from quasiparticle loss (see Section 6.1), one possible explanation would be that since large capacitor pads contain more Cooper pairs, then more Cooper pairs are broken by  $B_{||}$  and thus more quasiparticles are produced, increasing this way quasiparticle loss. This effect is supported by the fact that all resonators are equally well aligned (see Figure 6.5 b)) and that this possible trend is not noticeable in the other chips, which have similar capacitor size.

As the parallel magnetic field increases the population of Cooper-pairs decrease.

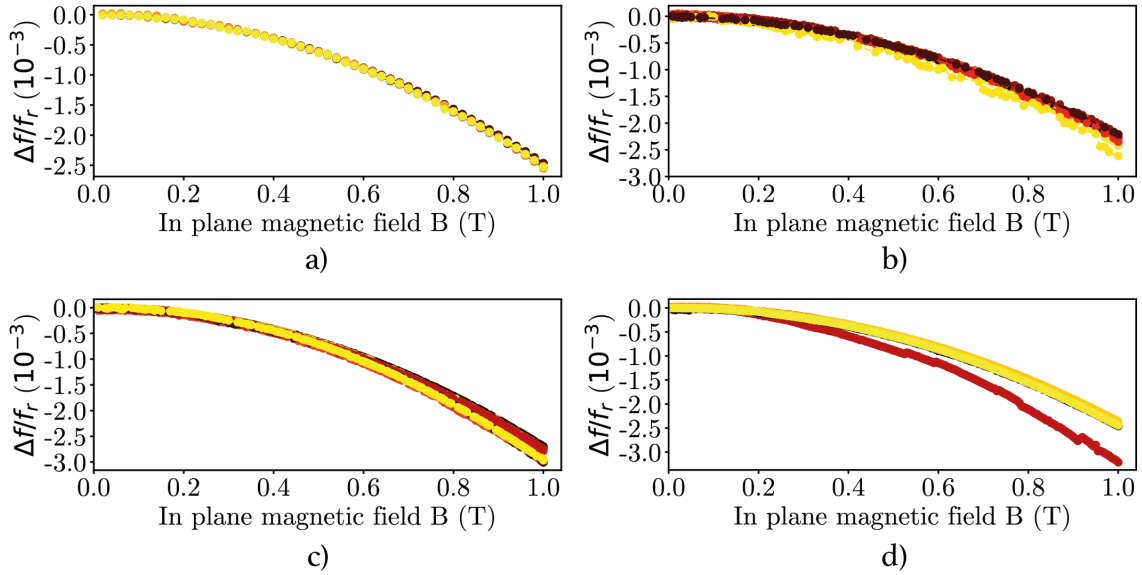


Figure 6.5: Relative resonance frequency with applied parallel magnetic field. a) Chip with varying inductor's width. Darker color marker corresponds to thinner inductor. b) Chip with varying capacitor's size. Darker marker color corresponds to smaller capacitor. c) Chip with varying capacitor's edge. Darker marker color corresponds to a more squared shape capacitor. d) Chip with varying inductor's width. Darker maker color corresponds to thinner inductor.

This effect translates into a higher kinetic inductance (c.f. Eqn. 2.20) and therefore a decreasing resonance frequency, since  $f_r = 1/\sqrt{L_k C}$ . Figure 6.5 shows the resonance frequency shift is quadratic, and can be fitted through:

$$\frac{\Delta f_r}{f_r} = \frac{f_r - f_r^0}{f_r} = -k_{\parallel} B_{\parallel}^2 \quad (6.2)$$

where  $f_r^0$  is the resonance frequency at zero field and  $k_{\parallel}$  a coefficient reflecting the Cooper-pair breaking of the external magnetic field. This coefficient can provide information on material's parameters if an analytic expression is derived. First we note that  $f_r \sim L_k^{-1/2}$ , and  $L_k \sim T_c^{-1}$  from equation 2.25. For small changes in frequency we have

$$\frac{f_r - f_r^0}{f_r} \approx \frac{1/\sqrt{L_k} - 1/\sqrt{L_k^0}}{1/\sqrt{L_k}} \approx -\frac{1}{2} \frac{\Delta L_k}{L_k^0} = \frac{1}{2} \frac{T_c - T_c^0}{T_c} \quad (6.3)$$

where we used the Taylor expansion at  $\Delta L_k = L_k - L_k^0 \approx 0$ :

$$\frac{1}{\sqrt{L_k}} = \frac{1}{\sqrt{L_k^0 + \Delta L_k}} \approx \frac{1}{\sqrt{L_k^0}} - \frac{\Delta L_k}{2\sqrt[3]{L_k^0}} + \dots \quad (6.4)$$

On the other hand, the Cooper-pair breaking strength is frequently characterized by the effective pair-breaking energy  $2\alpha$  [13]. An applied magnetic field reduces the critical temperature  $T_c$  linearly in  $\alpha$  as  $k_B(T_c - T_c^0) = -\pi\alpha/4$ . In the thin film parallel field approximation,  $T_c$  and  $\alpha$  are related through [13]:

$$\alpha = \frac{1}{6} \frac{De^2t^2}{\hbar} B_{||}^2 \rightarrow k_B(T_c - T_c^0) = -\frac{\pi}{24} \frac{De^2t^2}{\hbar} B_{||}^2 \quad (6.5)$$

where  $D$  is the electron diffusion constant of the material and  $t$  the thin film thickness. Combining Eqn. 6.3 with Eqn. 6.5 we obtain the final expression:

$$\frac{\Delta f_r}{f_r} = -\frac{\pi}{48} \frac{De^2t^2}{\hbar k_B T_c} B_{||}^2 \quad (6.6)$$

Which indicates a quadratic shift of the resonance frequency with the parallel magnetic field with parabolic coefficient  $k_{||} = (\pi/48)[De^2t^2/\hbar k_B T_c]$ . The quadratic behaviour depends on the superconducting film thickness (20 nm), the critical temperature of the superconducting film ( $T_c \approx 10$  K [52]) and the electron diffusion constant of the material ( $D$ ). We make use of Eqn. 6.6 and the measured resonance frequencies shown in Figure 6.5 to extract  $D \approx 0.56$  cm<sup>2</sup> s<sup>-1</sup>, consistent with previous studies with the same material [10] [61].

#### 6.4.2 Perpendicular Magnetic Field

Further insight into the effect of resonator geometry on  $Q_i$  can be achieved by orienting the field perpendicular to the sample plane. Figure 6.6 shows the dependence of  $Q_i$  in four different chips with different resonator geometry. In particular, Figures 6.6 a) and d) show that the thinnest inductors (the darkest color markers) are the most resilient to perpendicular magnetic field. This effect may be a result of the fewer number of magnetic induced vortices that fit in the inductor, and corresponding fewer vortex-induced losses. Secondly, Figure 6.6 b) shows that the smaller the capacitor, the most resilient is the resonator to out of plane fields. It must be noted that despite having the widest inductor ( $\sim 50$  nm wider due to fabrication inhomogeneities), the smallest capacitor maintains its enhanced performance (see Fig. 6.7 b)). This effect may be related to the fact that small capacitor pads contain less magnetic induced vortices. The shape of the capacitor (squared or circular) does not play a significant role in resonator's resilience, as shown in Figure 6.6 c). The typical

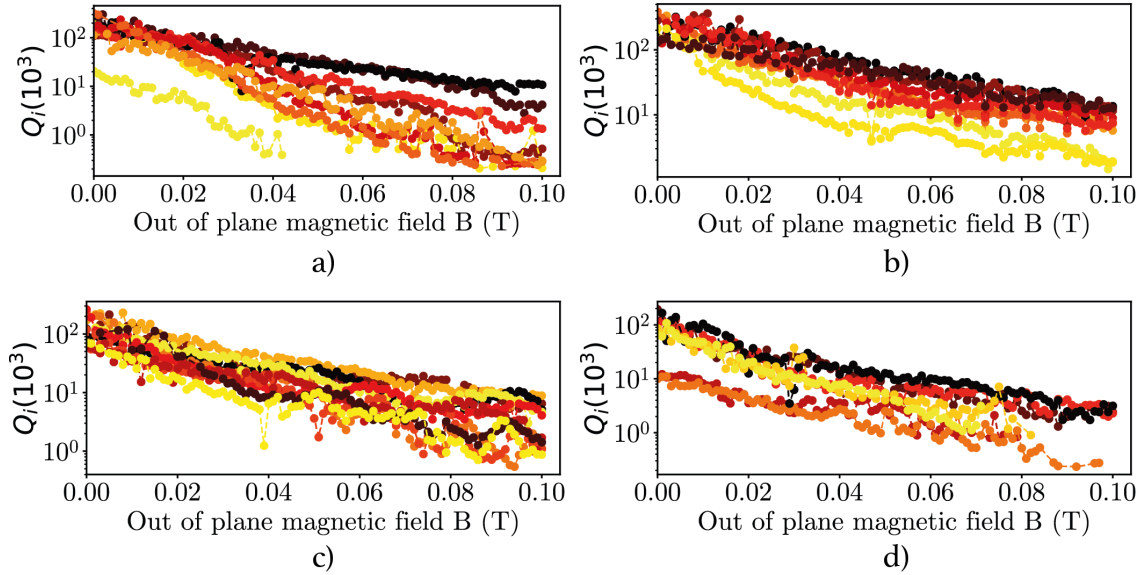


Figure 6.6: Intrinsic quality factor with applied perpendicular magnetic field. a) Chip with varying inductor's width. Darker color marker corresponds to thinner inductor. b) Chip with varying capacitor's size. Darker marker color corresponds to smaller capacitor. c) Chip with varying capacitor's edge. Darker marker color corresponds to a more squared shape capacitor. d) Chip with varying inductor's width. Darker maker color corresponds to thinner inductor.

dip in  $Q_i$  due to coupling of the resonator with magnetic impurities in the silicon substrate has been previously observed at  $B_{\perp} \sim 100$  mT[11] and therefore should be beyond the range of measurements.

The frequency shift of the resonators with perpendicular magnetic field follows a quadratic behaviour:

$$\frac{\Delta f_r}{f_r} = -k_{\perp} B_{\perp}^2 \quad (6.7)$$

where the parabolic coefficient now depends on the inductor's width  $W_r$  as:

$$\frac{\Delta f_r}{f_r} = -\frac{\pi}{48} \frac{De^2 W_r^2}{\hbar k_B T_c} B_{\perp}^2 \quad (6.8)$$

where the critical temperature depends on the superconducting material's thickness, and the rest comprise physical constants and a material related parameter ( $D$ ). The frequency shift dependence on the inductor's width is clearly depicted in Figures 6.7 a) and d), where the thinnest inductors (darkest color markers) have a lower

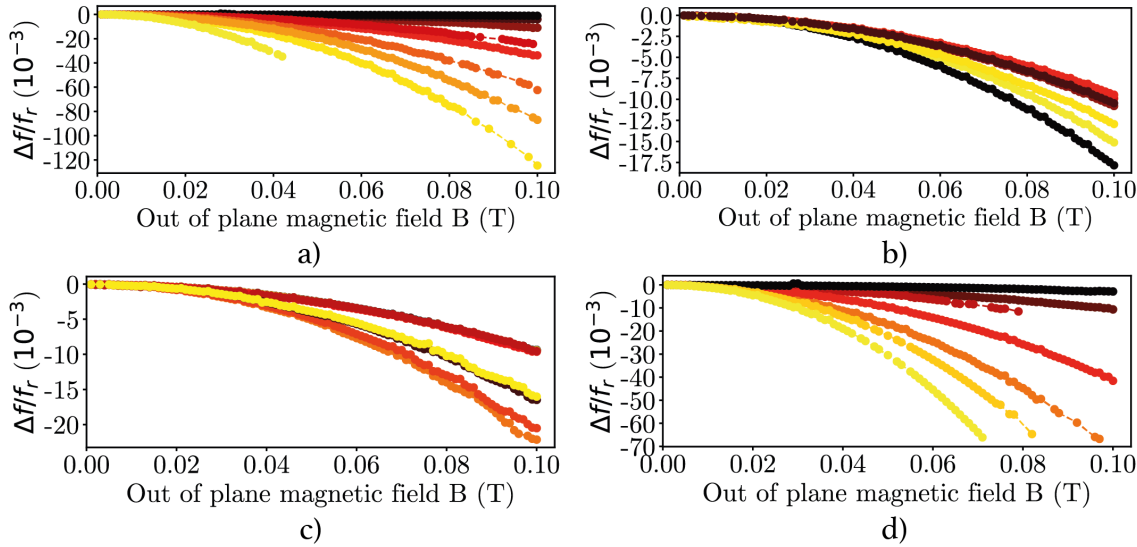


Figure 6.7: Relative resonant frequency with applied perpendicular magnetic field. a) Chip with varying inductor's width. Darker color marker corresponds to thinner inductor. b) Chip with varying capacitor's size. Darker marker color corresponds to smaller capacitor. c) Chip with varying capacitor's edge. Darker marker color corresponds to a more squared shape capacitor. d) Chip with varying inductor's width. Darker maker color corresponds to thinner inductor.

parabolic coefficient. In these figures we can observe how some of the wide inductors are not resilient up to 100 mT and therefore their corresponding resonances vanish with increasing out of plane field.

Figures 6.7 b),c) support the observation that the fabricated inductors have slightly different widths than initially intended due to fabrication factors difficult to control. This phenomena can become a useful additional tool when trying to identify resonators in the frequency spectrum, once the SEM inspection of the measured device has been done. Nevertheless, it can be seen that all resonator configurations with an inductor's width  $W \approx 200 \text{ nm} \pm 10 \text{ nm}$  are resilient up to at least 100 mT.

# Chapter 7

## Conclusions and further research

In this work we present the design, fabrication and characterization of magnetic field resilient lumped element resonators. We use the power dependence of resonators to extract their main loss mechanisms, and then analyze the role of geometry in resonator losses. Then we study the performance of all resonators under in plane and out of plane magnetic fields and obtain the optimum geometries for high-resilience resonators.

First, we find no clear correlation between  $Q_i$  and resonator's geometry at zero field within measurement variability, although thin inductors might origin higher quality factors. Further characterization of this trend is needed. The  $Q_i$  dependence with photon number in the resonator suggests that at powers high enough to saturate TLS systems, wide inductors are more susceptible to input power than thin inductors. We propose that the quasiparticle loss due to microwave induced cooper pair breaking is the main origin of that phenomenon. Wide inductors may contain a larger number of quasiparticles than thin inductors, therefore the multiplication process inherent of quasiparticle loss may be enhanced. The size and shape of the capacitor does not seem to play a significant role in the resonator's loss power dependence, which may stem from the fact that unsaturated TLS is not the main loss form of our resonators, type of loss that has been associated with the capacitance of the resonator [6].

In the presence of an applied in plane magnetic field, small capacitors appear to perform better than large capacitors as the field increases. This phenomena may be associated to quasiparticle loss, since on average large capacitors will contain more Cooper pairs, and the more Cooper pairs broken by the applied field the more quasiparticles will be produced. The in plane magnetic field does not seem to affect the rest of the geometries in any conclusive way, but remains a useful tool to ensure all resonators are properly aligned with the applied field. The small cross section of thinner inductors minimize the number of Abrikosov vortices present in the inductor

and therefore make resonators more resilient to the out of plane magnetic field, in agreement with previous studies [10][11]. The same reasoning can be applied to the size of the capacitor, for which we observe that small capacitors make the resonators more resilient to the out of plane field. However the shape of the capacitor does not play a role in the resonator's performance.

In this work the coupling quality factor was designed to be slightly lower than the internal quality factor at zero field, such that when the  $Q_i$  decreases for increasing applied magnetic fields the signal can still be accurately measured [6] [1]. Nonetheless when we study the power dependence of all resonators at zero field, we find that the condition  $Q_c < Q_i$  does not allow the photon number in resonators to vary with  $Q_i$ , since  $Q_T \approx Q_c$ . Therefore if loss characterization is aimed through power dependence measurements, it is warranted to have a better matching between  $Q_c$  and  $Q_i$ .

After several fabrication iterations of this resonator design, we learnt that in order to more accurately define the meander inductor, the whole resonator gap needs to be patterned using fine beam electron lithography and proximity error correction. Moreover, additional cleaning steps before applying lithography resist proved to produce better fabricated resonators.

## 7.1 Outlook

Different experiments can be made to gain further insight in superconducting resonators loss mechanisms. In this work we focused on geometry, in particular the inductor's width, capacitor's size and shape. The gap between the capacitor and the ground planes requires further investigation, since our measurements were unreliable and inconclusive. In addition, a comparison between one and multiple capacitor pads could be studied. By inserting a dielectric layer between the superconducting film and the substrate we could further investigate TLS dissipation, and thus analyze the role of the capacitor's geometry in resonator losses. One way to mitigate TLS losses from the substrate could stem from replacing our planar capacitor by a parallel plate capacitor, confining this way the electric field between the capacitor plates. Finally, varying the film thickness could give a deeper understanding of the losses trade-off.

Geometry aside, different superconducting materials such as ALD TiN and granular aluminum could be used. This could pave the way towards a better understanding of resonator geometry regardless of the material. Moreover, the performance of our lumped element resonators in different material platforms would provide a simple way to study the dependence of the kinetic inductance in different materials. Following this line of work, the current dependence of the kinetic inductance could be analyzed by incorporating a loop in the resonator and sending flux through it.

# Appendix A

## Coupling Quality factor

Here we present the derivation of the coupling quality factor of a resonator coupled to a feedline through a capacitance  $C_c$ . Note that we neglect internal losses. In order to simplify calculations we need to simplify the initial circuit illustrated in Figure A.1 a) [62].

The first step consists in doing the Norton equivalent of the initial circuit (c.f. A.1 b)). The new configuration results in the source and load impedances being in parallel, hence we can add them up (c.f. A.1 c)). Next, we do the Thevenin equivalent of the current circuit to obtain an LC resonator coupled to a voltage source. Then, we aim to obtain an equivalent circuit with the coupling capacitance in parallel with the LC system. We start by doing the Norton equivalent of circuit d). Following Norton theorem, we shortcircuit the voltage source and find the input impedance. This input impedance comprises a resistor in series with a capacitor:

$$Z_{in} = \frac{Z_0}{2} + \frac{1}{j\omega C_c} \quad (\text{A.1})$$

We can rewrite the input impedance in such a way that is equivalent to the same capacitor in parallel with a certain impedance  $Z_x$ :

$$Z_{in}^{-1} = \frac{1}{Z_x} + j\omega C_c \quad (\text{A.2})$$

We consider the domain bounded by  $\omega C_c Z_0 \ll 1$  and  $\omega C_c Z_x \gg 1$ . In this regime the effective impedance reads:

$$Z_x \approx \frac{2}{Z_0(\omega C_c)^2} \quad (\text{A.3})$$

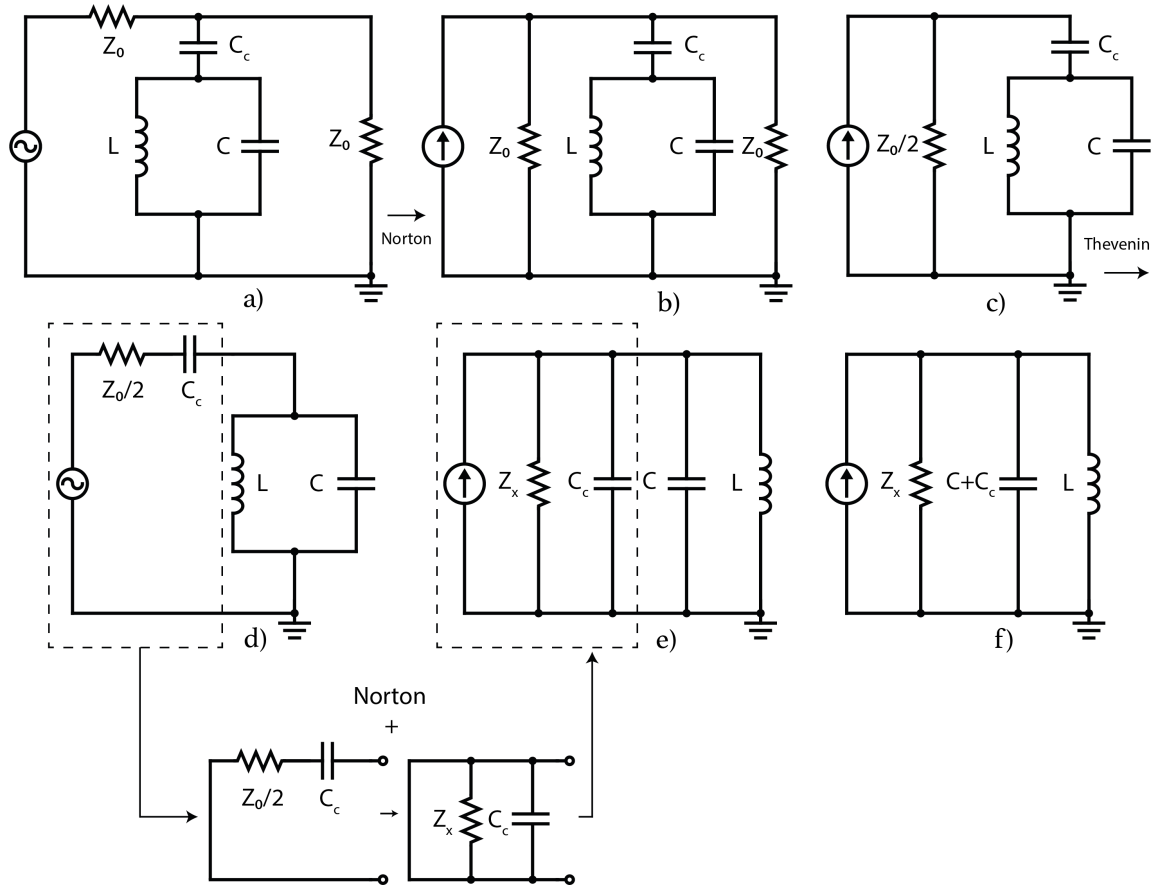


Figure A.1: a) Initial circuit with resonator capacitively coupled to a feedline. b) Norton equivalent of initial circuit. c) Simplification of the parallel impedances. d) Thevenin of the previous circuit. e) Norton equivalent and equivalent circuit transformation. f) Final simplified circuit.

Finally, we calculate the coupling quality factor with its fundamental definition (c.f. Eqn. 3.31):

$$Q_c = \omega_0 C_T Z_x = \sqrt{\frac{C_T}{L}} \frac{1}{\omega_0^2 C_c^2 (Z_0/2)} \quad (\text{A.4})$$

with  $C_T = C + C_c$  the total capacitance,  $\omega_0 = 1/\sqrt{LC_T}$  the resonance frequency and  $Z_0$  the impedance of the input/output lines.

# Appendix B

## Fabrication recipe

In this section we describe the fabrication steps necessary to fabricate our NbTiN multi-resonator sample.

### B.1 Wafer

#### B.1.1 Deposition

The substrate below our superconductor is a HiRes silicon wafer of  $525\ \mu\text{m}$ . Before sputtering our superconductor, we clean the wafer properly with a  $\text{HNO}_3$  bath (1 min) and posterior water soaking. Then we place the wafer in a beaker with HF for 5 minutes and rinse the wafer with water twice. After that we quickly move the wafer to the HMDS (that neutralizes the radicals so that the surface does not oxidize that quick) [9]. After the HMDS processing we move the wafer to the sputtering station.

NbTiN thin films were deposited by DC reactive magnetron sputtering in a high-vacuum deposition chamber (AJA International, Inc.). We achieve a NbTi plasma at room temperature with a fixed flow of Ar and N and let it active for 45 seconds, after which we put the shutter on. At the end of this process we should have a 20nm NbTiN thin film on top of the HiRes Si wafer. We can get an estimate on the kinetic inductance of the film by measuring the resistance with a 4 probe resistance meter and using equation 2.25 [19].

#### B.1.2 Markers

Next we apply titanium and palladium markers that will be used as coordinates references for the electron beam lithography. Finally we dice the sample in 1.5 cm by 1.5 cm samples.

## B.2 Chip

### B.2.1 Sample cleaning

Before anything else, we properly clean the sample by leaving it in a beaker filled with acetone at 50 °C for one hour with a magnetic spinner at constant angular velocity. Then the sample is placed in a beaker filled with PRS-3000 at 80 °C and a magnetic spinner for three hours. Next we rinse the sample with water twice, soak it in IPA and dry it out with a nitrogen gun.

### B.2.2 Lithography

We apply CSAR 09 ebeam resist on the sample through spin coating at 4000rpm and 5 minutes of baking at 185 °C. After the proper sample tilt and rotation alignment, the sample is loaded in the Raith EBPG-5200. The design is patterned in the resist via three different beams: fine, medium, and coarse. Each one of them with an appropriate dose selected through different dose tests.

### B.2.3 Development

After the electron beam lithography is done, we place the samples in a teflon holder and introduce them to the beakers according to the sequence:

- Amylacetate: 1 min
- MIBK:IPA: 1:3 1 min
- IPA to stop development
- Nitrogen gun

### B.2.4 Dry Etching

We etch 20 nm by 7 mm of NbTiN with a mixed plasma of SF<sub>6</sub> and O<sub>2</sub> in Sentech Etchlab 200 for 47 seconds.

### B.2.5 Dicing

We strip the dicing resist using ARS 600-71 for three hours. Then we apply dicing resist through spin coating at 1000 rpm and baking at 90 °C for 5 minutes. Finally two 2 mm by 7 mm chips are diced from the every sample.

### B.2.6 Wire Bonding

The sample is bonded to a Printed Circuit Board (PCB) through aluminum wires of  $25 \mu\text{m}$  of diameter.

### B.2.7 Optical micrographs

Figure B.1 shows an optical micrograph of every fabricated chip just before wire bonding.

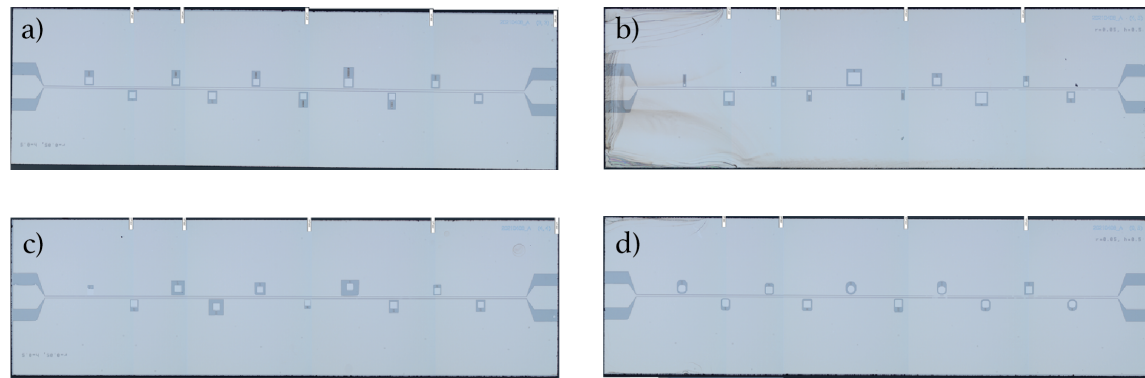


Figure B.1: Fabricated chips, thin film of NbTiN coloured in light blue, HiRes silicon substrate in dark blue. Each chip is 2 mm by 7 mm and contains 10 resonators. a) Chip with varying inductor's width. b) Chip with varying capacitor's size. c) Chip with varying resonator's gap. d) Chip with varying capacitor's pad edge radius.

### B.2.8 SEM inspection

Here we show different SEM inspections to illustrate the change in resonator design within the same chip.

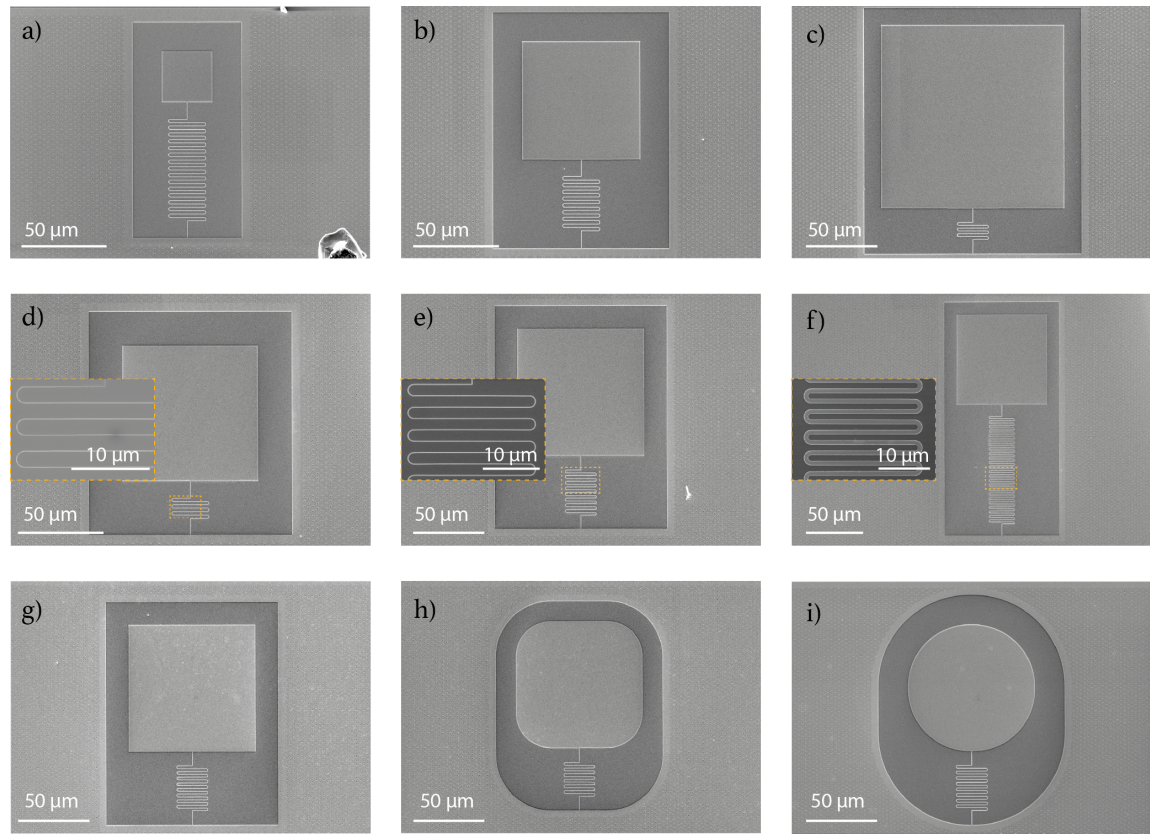


Figure B.2: SEM figures of resonators with varying capacitor's size: a) $L_r=30\text{ }\mu\text{m}$ , b) $L_r=70\text{ }\mu\text{m}$ , c) $L_r=130\text{ }\mu\text{m}$ . SEM figures of resonators with varying inductor's width: d) $W_r=0.1\text{ }\mu\text{m}$ , e) $W_r=0.2\text{ }\mu\text{m}$ , f) $W_r=1.0\text{ }\mu\text{m}$ . Insets show a zoom in of the inductor. SEM figures of resonators with varying edge radius: g) $R_r=0\text{ }\mu\text{m}$ , h) $R_r=25\text{ }\mu\text{m}$ , i) $R_r=45\text{ }\mu\text{m}$ .

# Appendix C

## Additional Measurements

In this chapter we show additional figures to complement results from the main measurement section.

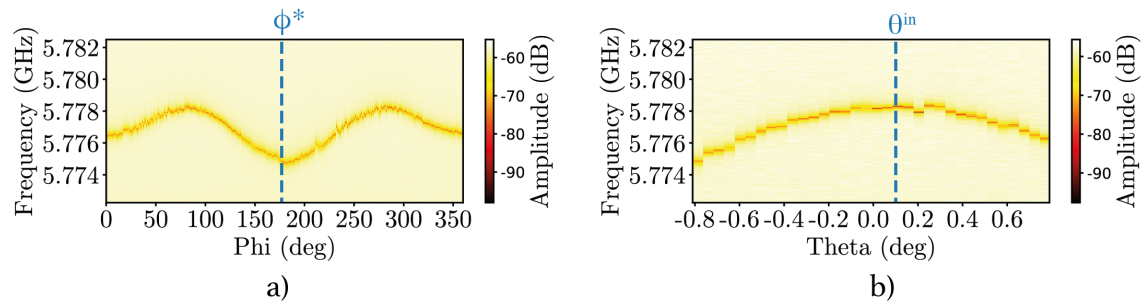


Figure C.1: Field alignment of  $0.6\ \mu\text{m}$  wide inductor resonator with  $f_r \approx 5.778\ \text{GHz}$  at a magnetic field magnitude of  $500\ \text{mT}$ . a) Magnetic field  $\phi$ -sweep (spherical coordinates) of the resonance frequency at  $\theta = 0.8^\circ$ . The lowest  $f_r$  at  $\phi = \phi^*$  (indicated with a dashed blue line) corresponds to the largest out of plane component. b) Magnetic field  $\theta$ -sweep (spherical coordinates) of the resonance frequency at  $\phi = \phi^* = 177.1^\circ$ . The highest  $f_r$  at  $\theta = \theta_{in}$  (indicated with a dashed blue line) corresponds to the largest in plane component.

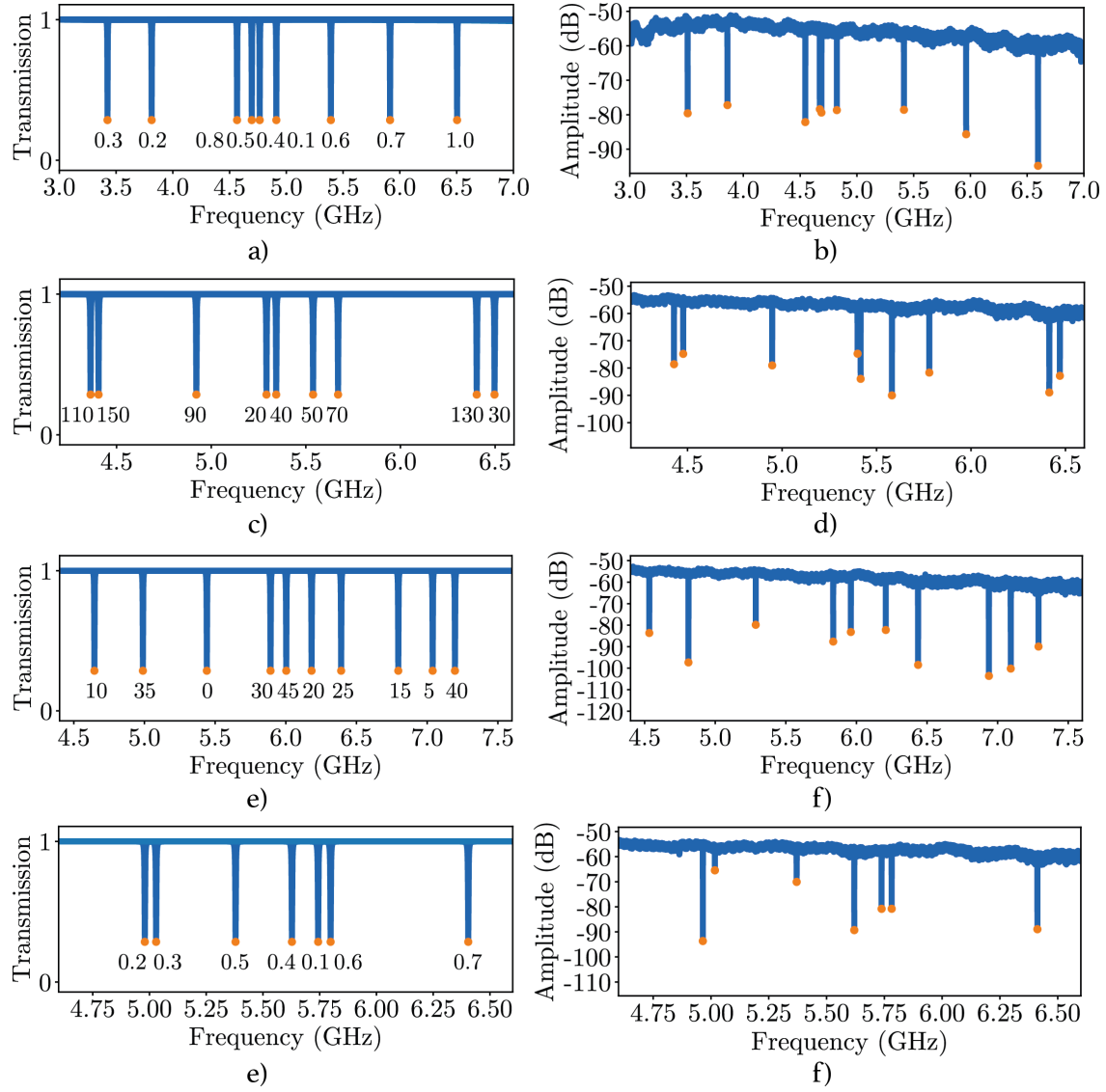


Figure C.2: Transmission comparison of chip in which we vary: a)b) inductor's width, c)d) capacitor's size, e)f) capacitor's shape, g)h) inductor's width. Left column corresponds to simulated resonances after SEM inspection of fabricated chip, while right column corresponds to measured resonances at drive power  $-20\text{dBm}$  (at the source output) and mixing chamber temperature of  $T \approx 25\text{mK}$ . The numbers below simulated resonances denote the geometric feature corresponding to that resonance, in  $\mu\text{m}$ .

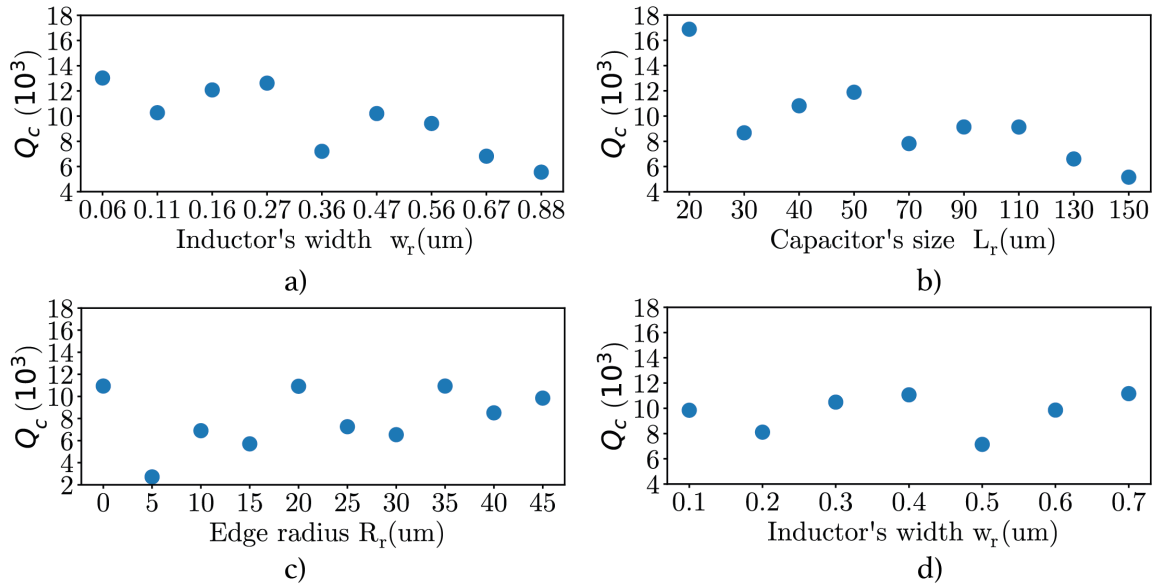


Figure C.3: Measured  $Q_c$  for each chip at  $-10 \text{ dBm}$  at the power source output. The errorbars estimated from the fit are smaller than data points. a) Chip with varying inductor's width. b) Chip with varying capacitor's size. c) Chip with varying capacitor's edge radius. d) Chip with varying inductor's width.

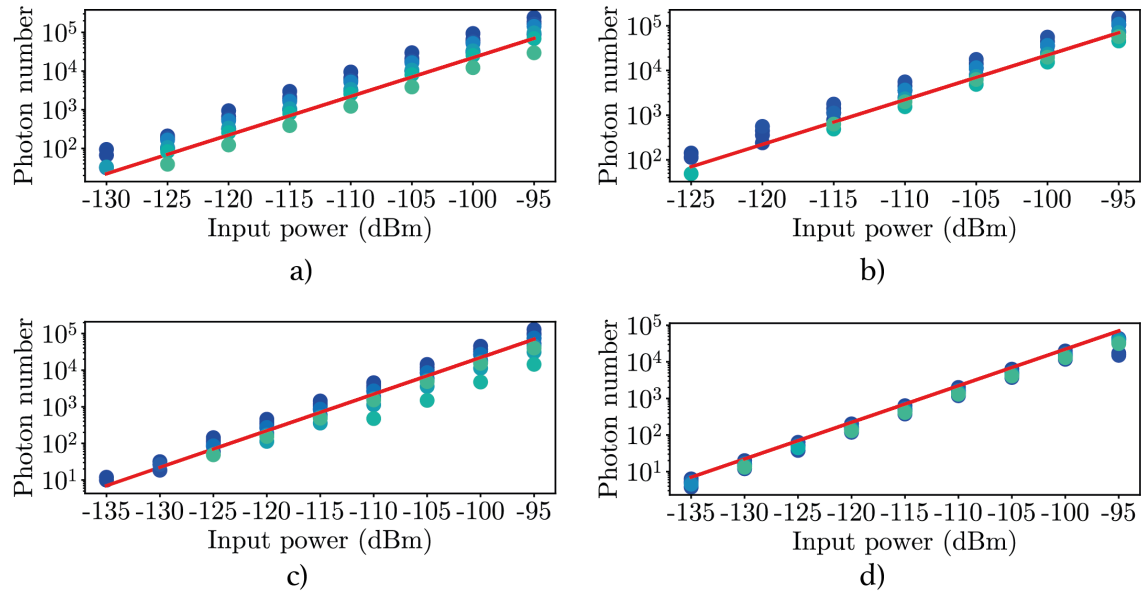


Figure C.4: Estimated photon number using equation 3.47 versus drive power. Darker blue corresponds to lower resonant frequency. Red line is a fit to show the single linear dependence of the photon number with input power. a) Chip with varying inductor's width. b) Chip with varying capacitor's size. c) Chip with varying capacitor's edge radius. d) Chip with varying inductor's width.

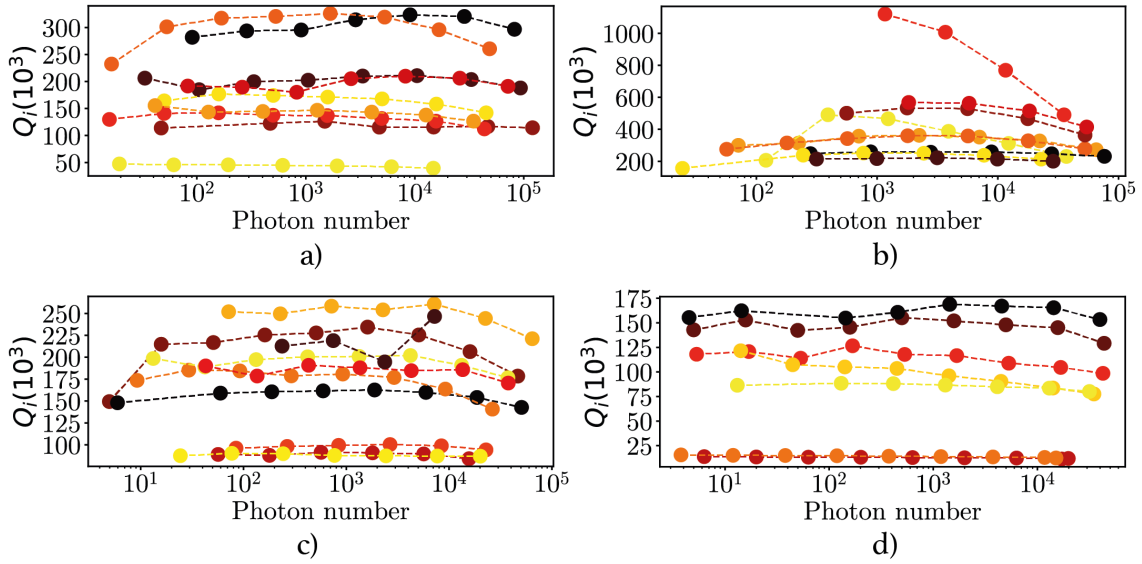


Figure C.5: Intrinsic quality factor versus photon number. a) Chip with varying inductor's width. Darker color marker corresponds to thinner inductor. b) Chip with varying capacitor's size. Darker marker color corresponds to smaller capacitor. c) Chip with varying capacitor's edge. Darker marker color corresponds to a more squared shape capacitor. d) Chip with varying inductor's width. Darker maker color corresponds to thinner inductor.

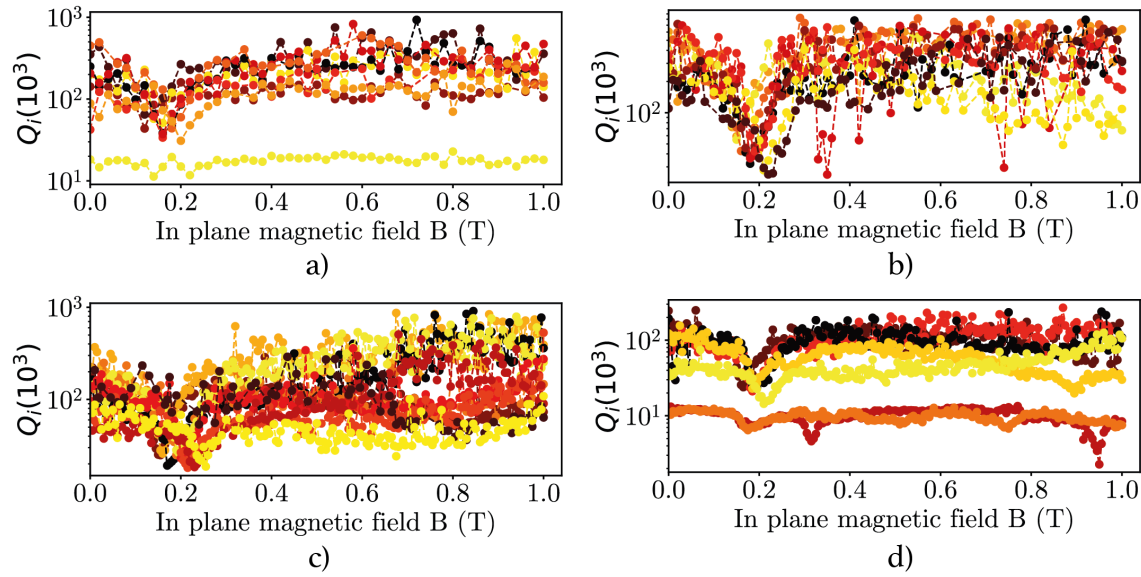


Figure C.6: Intrinsic quality factor with increasing parallel magnetic field. a) Chip with varying inductor's width. Darker color marker corresponds to thinner inductor. b) Chip with varying capacitor's size. Darker marker color corresponds to smaller capacitor. c) Chip with varying capacitor's edge. Darker marker color corresponds to a more squared shape capacitor. d) Chip with varying inductor's width. Darker maker color corresponds to thinner inductor.

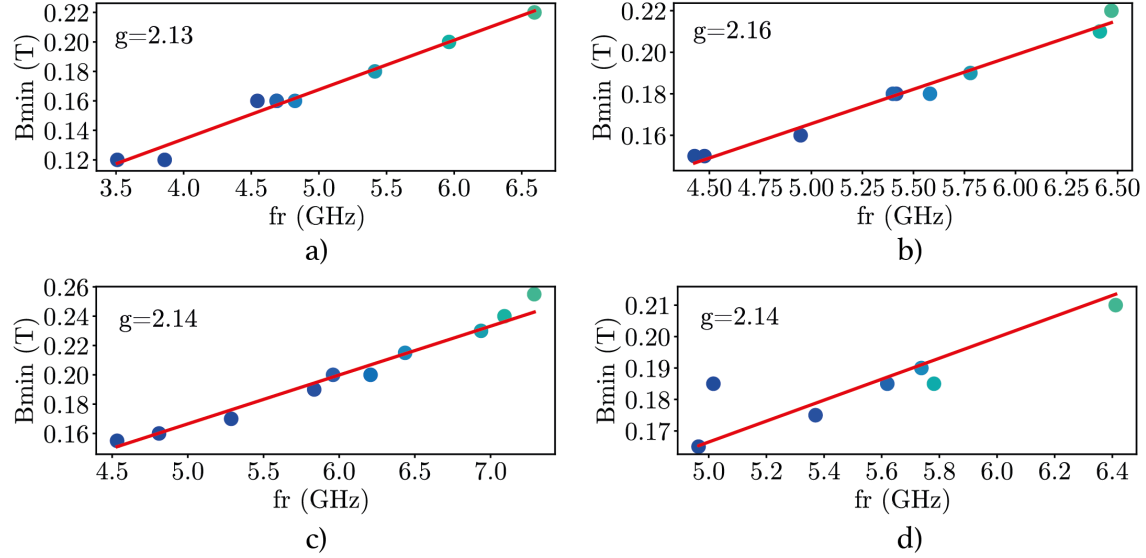


Figure C.7: Dip of parallel magnetic field versus resonant frequency. The darker the color markers the lower the frequency of the corresponding resonator. The red line corresponds to the average  $g$ -factor of all resonators of the same chip. a) Chip with varying inductor's width. b) Chip with varying capacitor's size. c) Chip with varying capacitor's edge. d) Chip with varying inductor's width.

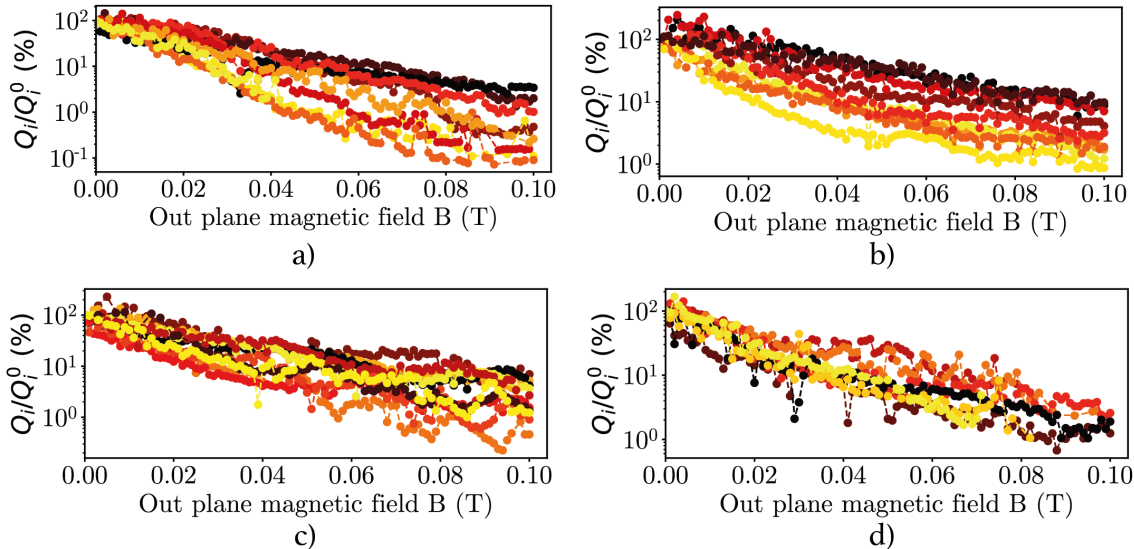


Figure C.8: Intrinsic quality factor divided by quality factor at zero field with increasing perpendicular magnetic field. a) Chip with varying inductor's width. Darker color marker corresponds to thinner inductor. b) Chip with varying capacitor's size. Darker marker color corresponds to smaller capacitor. c) Chip with varying capacitor's edge. Darker marker color corresponds to a more squared shape capacitor. d) Chip with varying inductor's width. Darker maker color corresponds to thinner inductor.

# Bibliography

- [1] Jiansong Gao. *The physics of superconducting microwave resonators*. California Institute of Technology, 2008.
- [2] Alexandre Blais, Ren-Shou Huang, Andreas Wallraff, Steven M Girvin, and R Jun Schoelkopf. Cavity quantum electrodynamics for superconducting electrical circuits: An architecture for quantum computation. *Physical Review A*, 69(6):062320, 2004.
- [3] Andreas Wallraff, David I Schuster, Alexandre Blais, Luigi Frunzio, R-S Huang, Johannes Majer, Sameer Kumar, Steven M Girvin, and Robert J Schoelkopf. Strong coupling of a single photon to a superconducting qubit using circuit quantum electrodynamics. *Nature*, 431(7005):162–167, 2004.
- [4] Matteo Mariantoni, Haiyan Wang, Takashi Yamamoto, Matthew Neeley, Radoslaw C Bialczak, Yu Chen, Mike Lenander, Erik Lucero, Aaron D O’Connell, Daniel Sank, et al. Implementing the quantum von neumann architecture with superconducting circuits. *Science*, 334(6052):61–65, 2011.
- [5] Max Hofheinz, H Wang, Markus Ansmann, Radoslaw C Bialczak, Erik Lucero, Matthew Neeley, AD O’connell, Daniel Sank, J Wenner, John M Martinis, et al. Synthesizing arbitrary quantum states in a superconducting resonator. *Nature*, 459(7246):546–549, 2009.
- [6] Corey Rae Harrington McRae, Haozhi Wang, Jiansong Gao, Michael R Vissers, Teresa Brecht, Andrew Dunsworth, David P Pappas, and Josh Mutus. Materials loss measurements using superconducting microwave resonators. *Review of Scientific Instruments*, 91(9):091101, 2020.
- [7] Jens Koch, M Yu Terri, Jay Gambetta, Andrew A Houck, David Isaac Schuster, Johannes Majer, Alexandre Blais, Michel H Devoret, Steven M Girvin, and Robert J Schoelkopf. Charge-insensitive qubit design derived from the cooper pair box. *Physical Review A*, 76(4):042319, 2007.

- [8] SP Harvey, CGL Böttcher, LA Orona, SD Bartlett, AC Doherty, and Amir Yacoby. Coupling two spin qubits with a high-impedance resonator. *Physical Review B*, 97(23):235409, 2018.
- [9] A Bruno, G De Lange, S Asaad, KL Van Der Enden, NK Langford, and L Di-Carlo. Reducing intrinsic loss in superconducting resonators by surface treatment and deep etching of silicon substrates. *Applied Physics Letters*, 106(18):182601, 2015.
- [10] JG Kroll, F Borsoi, KL Van Der Enden, W Uilhoorn, D De Jong, M Quintero-Pérez, DJ Van Woerkom, A Bruno, SR Plissard, D Car, et al. Magnetic-field-resilient superconducting coplanar-waveguide resonators for hybrid circuit quantum electrodynamics experiments. *Physical Review Applied*, 11(6):064053, 2019.
- [11] Nodar Samkharadze, A Bruno, Pasquale Scarlino, G Zheng, DP DiVincenzo, L DiCarlo, and LMK Vandersypen. High-kinetic-inductance superconducting nanowire resonators for circuit qed in a magnetic field. *Physical Review Applied*, 5(4):044004, 2016.
- [12] Marta Pita-Vidal, Arno Bargerbos, Chung-Kai Yang, David J Van Woerkom, Wolfgang Pfaff, Nadia Haider, Peter Krogstrup, Leo P Kouwenhoven, Gijs De Lange, and Angela Kou. Gate-tunable field-compatible fluxonium. *Physical Review Applied*, 14(6):064038, 2020.
- [13] Michael Tinkham. *Introduction to superconductivity*. Courier Corporation, 2004.
- [14] Walther Meissner and Robert Ochsenfeld. Ein neuer effekt bei eintritt der supraleitfähigkeit. *Naturwissenschaften*, 21(44):787–788, 1933.
- [15] NW Ashcroft and ND Mermin. Solid state physics, college edn. *Thomson Learning Inc*, 1976.
- [16] Fritz London and Heinz London. The electromagnetic equations of the superconductor. *Proceedings of the Royal Society of London. Series A-Mathematical and Physical Sciences*, 149(866):71–88, 1935.
- [17] Cornelis Jacobus Gorter and Hendrik Casimir. On supraconductivity i. *Physica*, 1(1-6):306–320, 1934.
- [18] Simon Doyle. *Lumped element Kinetic Inductance Detectors*. PhD Thesis, Cardiff University, 2008.

- [19] Anthony Joseph Annunziata. *Single-photon detection, kinetic inductance, and non-equilibrium dynamics in niobium and niobium nitride superconducting nanowires*. Yale University, 2010.
- [20] Edward Bennett Rosa. *The self and mutual inductances of linear conductors*. Number 80. US Department of Commerce and Labor, Bureau of Standards, 1908.
- [21] John Bardeen, Leon N Cooper, and John Robert Schrieffer. Theory of superconductivity. *Physical review*, 108(5):1175, 1957.
- [22] Anthony J Annunziata, Daniel F Santavicca, Luigi Frunzio, Gianluigi Catelani, Michael J Rooks, Aviad Frydman, and Daniel E Prober. Tunable superconducting nanoinductors. *Nanotechnology*, 21(44):445202, 2010.
- [23] PD Mauskopf. Transition edge sensors and kinetic inductance detectors in astronomical instruments. *Publications of the Astronomical Society of the Pacific*, 130(990):082001, 2018.
- [24] Koki Watanabe, Keiji Yoshida, and Takeshi Aoki Kohjiro. Kinetic inductance of superconducting coplanar waveguides. *Japanese journal of applied physics*, 33(10R):5708, 1994.
- [25] Keiji Yoshida, K Watanabe, T Kisu, and K Enpuku. Evaluation of magnetic penetration depth and surface resistance of superconducting thin films using coplanar waveguides. *IEEE Transactions on Applied Superconductivity*, 5(2):1979–1982, 1995.
- [26] Spartak Gevorgian, LJ Peter Linner, and Erik L Kollberg. Cad models for shielded multilayered cpw. *IEEE transactions on microwave theory and techniques*, 43(4):772–779, 1995.
- [27] P W Anderson, Bertrand I Halperin, and C M Varma. Anomalous low-temperature thermal properties of glasses and spin glasses. *Philosophical Magazine*, 25(1):1–9, 1972.
- [28] Clemens Müller, Jared H Cole, and Jürgen Lisenfeld. Towards understanding two-level-systems in amorphous solids: insights from quantum circuits. *Reports on Progress in Physics*, 82(12):124501, 2019.
- [29] William A Phillips. Two-level states in glasses. *Reports on Progress in Physics*, 50(12):1657, 1987.

- [30] John M Martinis, Ken B Cooper, Robert McDermott, Matthias Steffen, Markus Ansmann, KD Osborn, Katarina Cicak, Seongshik Oh, David P Pappas, Raymond W Simmonds, et al. Decoherence in josephson qubits from dielectric loss. *Physical review letters*, 95(21):210503, 2005.
- [31] Jiansong Gao, Miguel Daal, John M Martinis, Anastasios Vayonakis, Jonas Zmuidzinas, Bernard Sadoulet, Benjamin A Mazin, Peter K Day, and Henry G Leduc. A semiempirical model for two-level system noise in superconducting microresonators. *Applied Physics Letters*, 92(21):212504, 2008.
- [32] Jiansong Gao, Miguel Daal, Anastasios Vayonakis, Shwetank Kumar, Jonas Zmuidzinas, Bernard Sadoulet, Benjamin A Mazin, Peter K Day, and Henry G Leduc. Experimental evidence for a surface distribution of two-level systems in superconducting lithographed microwave resonators. *Applied Physics Letters*, 92(15):152505, 2008.
- [33] Chunhua Song, Thomas W Heitmann, Michael P DeFeo, Kang Yu, Robert McDermott, Matthew Neeley, John M Martinis, and Britton LT Plourde. Microwave response of vortices in superconducting thin films of re and al. *Physical Review B*, 79(17):174512, 2009.
- [34] DJ Goldie and S Withington. Non-equilibrium superconductivity in quantum-sensing superconducting resonators. *Superconductor Science and Technology*, 26(1):015004, 2012.
- [35] PJ De Visser, DJ Goldie, P Diener, S Withington, JJA Baselmans, and TM Klapwijk. Evidence of a nonequilibrium distribution of quasiparticles in the microwave response of a superconducting aluminum resonator. *Physical review letters*, 112(4):047004, 2014.
- [36] R-P Riwar and Gianluigi Catelani. Efficient quasiparticle traps with low dissipation through gap engineering. *Physical Review B*, 100(14):144514, 2019.
- [37] Jan Goetz, Frank Deppe, Max Haeberlein, Friedrich Wulschner, Christoph W Zollitsch, Sebastian Meier, Michael Fischer, Peter Eder, Edwar Xie, Kirill G Fedorov, et al. Loss mechanisms in superconducting thin film microwave resonators. *Journal of Applied Physics*, 119(1):015304, 2016.
- [38] Jeremy M Sage, Vladimir Bolkhovsky, William D Oliver, Benjamin Turek, and Paul B Welander. Study of loss in superconducting coplanar waveguide resonators. *Journal of Applied Physics*, 109(6):063915, 2011.

- [39] S Ohya, B Chiaro, A Megrant, C Neill, R Barends, Y Chen, J Kelly, D Low, J Mutus, PJJ O’Malley, et al. Room temperature deposition of sputtered tin films for superconducting coplanar waveguide resonators. *Superconductor Science and Technology*, 27(1):015009, 2013.
- [40] Greg Calusine, Alexander Melville, Wayne Woods, Rabindra Das, Corey Stull, Vlad Bolkhovsky, Danielle Braje, David Hover, David K Kim, Xhovalin Miloshi, et al. Analysis and mitigation of interface losses in trenched superconducting coplanar waveguide resonators. *Applied Physics Letters*, 112(6):062601, 2018.
- [41] C Neill, A Megrant, R Barends, Yu Chen, B Chiaro, J Kelly, JY Mutus, PJJ O’Malley, D Sank, J Wenner, et al. Fluctuations from edge defects in superconducting resonators. *Applied Physics Letters*, 103(7):072601, 2013.
- [42] David M Pozar. *Microwave engineering*. John wiley & sons, 2011.
- [43] Inder Jit Bahl. *Lumped elements for RF and microwave circuits*. Artech house, 2003.
- [44] Rami Barends. Photon-detecting superconducting resonators. 2009.
- [45] M Stoutimore Khalil, MJA Stoutimore, FC Wellstood, and KD Osborn. An analysis method for asymmetric resonator transmission applied to superconducting devices. *Journal of Applied Physics*, 111(5):054510, 2012.
- [46] Goran Stojanović, Ljiljana Živanov, and Mirjana Damjanović. Compact form of expressions for inductance calculation of meander inductors. *Serbian journal of electrical engineering*, 1(3):57–68, 2004.
- [47] Gheorghe Stan, Stuart B Field, and John M Martinis. Critical field for complete vortex expulsion from narrow superconducting strips. *Physical review letters*, 92(9):097003, 2004.
- [48] KH Kuit, JR Kirtley, W Van Der Veur, CG Molenaar, FJG Roesthuis, AGP Troeman, JR Clem, H Hilgenkamp, Horst Rogalla, and Jakob Flokstra. Vortex trapping and expulsion in thin-film yba 2 cu 3 o 7-  $\delta$  strips. *Physical Review B*, 77(13):134504, 2008.
- [49] Chunhua Song, Michael P DeFeo, Kang Yu, and Britton LT Plourde. Reducing microwave loss in superconducting resonators due to trapped vortices. *Applied Physics Letters*, 95(23):232501, 2009.

- [50] Daniel Bothner, Tobias Gaber, Matthias Kemmler, Dieter Koelle, and Reinhold Kleiner. Improving the performance of superconducting microwave resonators in magnetic fields. *Applied Physics Letters*, 98(10):102504, 2011.
- [51] AWR-Cadence. Microwave office, 2022. URL <https://www.awr.com/>.
- [52] Marta Pita-Vidal. Development of nanowire-based fluxonium devices. 2019.
- [53] COMSOL. Comsol multiphysics, 2022. URL <https://www.comsol.com/>.
- [54] Daniel C Mattis and John Bardeen. Theory of the anomalous skin effect in normal and superconducting metals. *Physical Review*, 111(2):412, 1958.
- [55] Sebastian Krinner, Simon Storz, Philipp Kurpiers, Paul Magnard, Johannes Heinsoo, Raphael Keller, Janis Luetolf, Christopher Eichler, and Andreas Wallraff. Engineering cryogenic setups for 100-qubit scale superconducting circuit systems. *EPJ Quantum Technology*, 6(1):2, 2019.
- [56] Centric RF. C4102 smp female to female coaxial blindmate "bullet" 0.254", 2022. URL <https://www.centricrf.com/adapters/smp-adapters/smp-to-smp-adapters/c4102-smp-female-to-female-coaxial-blindmate-bullet-0-254/>.
- [57] Jochem Baselmans, Stephen Yates, Pascale Diener, and Pieter de Visser. Ultra low background cryogenic test facility for far-infrared radiation detectors. *Journal of Low Temperature Physics*, 167(3):360–366, 2012.
- [58] Laird. Eccosorb hr, 2022. URL <https://www.laird.com/products/microwave-absorbers/microwave-absorbing-foams/eccosorb-hr>.
- [59] James W Lamb. Miscellaneous data on materials for millimetre and submillimetre optics. *International Journal of Infrared and Millimeter Waves*, 17(12):1997–2034, 1996.
- [60] Jonas Zmuidzinas. Superconducting microresonators: Physics and applications. *Annu. Rev. Condens. Matter Phys.*, 3(1):169–214, 2012.
- [61] Mariia Sidorova, AD Semenov, H-W Hübers, Samuel Gyger, Stephan Steinhauer, X Zhang, and A Schilling. Magnetoconductance and photoresponse properties of disordered nbtin films. *Physical Review B*, 104(18):184514, 2021.
- [62] David Isaac Schuster. *Circuit quantum electrodynamics*. Yale University, 2007.